Melting of Garnet Peridotite and the Origin of Komatiite and Depleted Lithosphere

MICHAEL J. WALTER*

INSTITUTE FOR STUDY OF THE EARTH'S INTERIOR, OKAYAMA UNIVERSITY, MISASA, TOTTORI-KEN 682-01, JAPAN

Melting experiments on fertile peridotite KR4003, a 'pyrolitic' composition, were made from 3 to 7 GPa in piston-cylinder and multi-anvil apparatus. Temperature gradients across the sample were minimized (<25°C), and the compositions of all phases were determined. Modal abundances of coexisting phases were calculated by mass balance, and the results were used to determine phase relations. Orthopyroxene is not stable at the solidus of garnet peridotite above ~3·3 GPa, but crystallizes above the solidus by incongruent melting of cpx. Melt compositions from 3 to 7 GPa (>10% melting) are picritic, komatiitic, and peridotitic. The Al_2O_3 content of partial melts decreases with increase in pressure because of an increase in garnet stability, providing a barometer for melting. The Al_2O_3 contents of komatiites indicate secular variation in the average pressure of melt segregation from residues, with early Archean komatiites and Cretaceous komatiites generated at the highest and lowest average pressures, respectively. The high CaO/Al_2O_3 ratios of Archean alumina undepleted komatiites (~0·9–1·5) require residual garnet if their sources were pyrolitic. Paradoxically, chondrite-normalized Gd/Yb of about unity in these komatiites precludes garnet involvement. Archean komatiite source regions may have had CaO/Al_2O_3 values of about 1·4 and 1·0 in the early and late Archean, respectively, significantly greater than the pyrolitic ratio of 0·8, whereas the source of Cretaceous komatiites may have had pyrolitic CaO/Al_2O_3. Thus, secular variations in this ratio are indicated. Chemical differences between coeval alumina undepleted and alumina depleted komatiites can be explained by melting at similar pressures, with alumina undepleted komatiites segregating from a garnet-free residue, and alumina depleted komatiites segregating from a garnet-bearing residue. Depleted, high-temperature peridotites from cratons, and oceanic peridotites, can be melting residues of pyrolitic mantle at low pressures (<3 GPa). Average low-temperature peridotite from the Siberian craton can be generated as a residue of komatiite melt extraction from a near-pyrolitic mantle at ~6 GPa and 40% melting. Average southern African low-temperature peridotite cannot be a melting residue of pyrolitic mantle.

However, it can be a residue of komatiite melt extraction at >7 GPa from a mantle enriched in SiO_2 relative to pyrolite.

INTRODUCTION

Melting of garnet peridotite is an important process in the genesis of a variety of magma types, including basalts, picrites, komatiites, and alkalic magmas such as kimberlites and carbonatites (e.g. Yoder, 1976; Wilson, 1989). Moreover, the depleted residues formed in the melting events that produce these magmas are important components of oceanic and cratonic lithosphere (e.g. Dick & Fisher, 1984; Boyd, 1989). An excellent way to understand the process of garnet peridotite melting is by experiment. A common experimental method, and the one followed here, is the forward approach whereby one determines the phase relations of 'natural' starting materials that serve as model compositions for the Earth's mantle. The advantage of this approach is that the results may be applied directly to melting in the mantle. The disadvantage is that multi-variant phase relations make the results specific to the chosen composition, and extrapolation of the results to other compositions can be ambiguous.

In this study, the phase relations for melting of peridotite composition KR4003 have been determined from 3 to 7 GPa. This peridotite is a sub-continental xenolith from West Kettle River, British Columbia; a geologic

*Tel: 81-858-43-1215. Fax: 81-858-43-3450. e-mail: walter@misasa. okayama-u.ac.jp

Table 1: Pyrolitic model mantle compositions

	1	2	3	4	5
SiO$_2$	44·9	44·5	45·0	45·2	44·7
TiO$_2$	0·16	0·16	0·20	0·22	0·15
Cr$_2$O$_3$	0·41	0·31	0·38	0·46	—
Al$_2$O$_3$	4·26	3·59	4·45	3·97	3·9
FeO	8·02	8·10	8·05	7·82	8·5
MgO	37·3	39·22	37·8	38·3	38·0
CaO	3·45	3·44	3·55	3·50	3·2
MnO	0·13	0·12	0·14	0·13	0·14
NiO	0·24	0·25	0·25	0·27	—
Na$_2$O	0·22	0·30	0·36	0·33	0·34
K$_2$O	0·09	0·02	0·03	0·03	0·03
Total	99·18	100·01	100·21	100·23	98·96
mg-no.*	89·2	89·6	89·3	89·7	88·9

1, West Kettle River spinel lherzolite xenolith used in this study [as given by Xue *et al*. (1990), except Ti, which has been determined by microprobe analysis of quenched melt]. 2, spinel lherzolite KLB-1 from Kilbourne's Hole (Takahashi, 1986). 3, pyrolite model of McDonough & Sun (1995). 4, least depleted ultramafic xenolith model of Jagoutz *et al*. (1979). 5, average Zabargad peridotite (Bonatti *et al*., 1986). *mg*-number calculated as molar ($Mg/Mg+Fe$) × 100 where $Fe^{2+}/(Fe^{2+} + Fe^{3+}) = 1$.

and geochemical description of this and associated xeno-liths has been given by Xue *et al.* (1990). KR4003 has a major element composition that puts it in a class of fertile compositions referred to commonly as 'pyrolitic' upper mantle. The composition of KR4003 is listed in Table 1, along with the compositions of other estimates for fertile upper mantle. KR4003 is close in composition to peridotite KLB-1 (Takahashi, 1986), and is very similar to pyrolite model compositions and to peridotites from Zabargad that may represent fertile oceanic upper mantle (Jagoutz *et al.*, 1979; McDonough & Sun, 1995; Bonatti *et al.*, 1986). Mantle of this nature is thought to be representative of primitive upper mantle, and perhaps the entire mantle (e.g. McDonough & Sun, 1995). There-fore, it is important to know the melting behavior of pyrolitic mantle, not only to test models for the origin of magmas and residues, but also to assess the suitability of pyrolite as a source material.

The compositions of melts generated from pyrolitic mantle have been determined with increasing precision in recent years at pressures up to 3 GPa (Falloon & Green, 1988; Kinzler & Grove, 1992*a*; Hirose & Kushiro, 1993; Baker & Stolper, 1994; Kushiro, 1996). Although much has been learned about the phase relations of pyrolite at pressures from 3 to >20 GPa with the advent of the multi-anvil apparatus (Takahashi & Scarfe, 1985; Takahashi, 1986; Herzberg *et al.*, 1990; Canil, 1992; Takahashi *et al.*, 1993; Zhang & Herzberg, 1994), tech-nical difficulties, associated mostly with high temperature gradients, have made it difficult to achieve the kind

of precise information on phase relations and phase compositions that has been obtained at lower pressures. In this study, the temperature gradient problem has been minimized, and new data for melting of pyrolitic mantle in the garnet stability field are presented. These data are applied to models for the generation of komatiite magmas, and to the origin of oceanic and cratonic peridotite.

EXPERIMENTAL MELTING OF GARNET LHERZOLITE
Philosophy

In many of the previously reported melting experiments on peridotite compositions made in multi-anvil apparatus, a large temperature gradient (>50–100°C/mm) existed across the samples and run durations were a few to tens of minutes (e.g. Takahashi & Scarfe, 1985; Herzberg *et al.*, 1990; Zhang & Herzberg, 1994). Large temperature gradients can have experimental advantages because an isobaric slice of a phase diagram from solidus to liquidus can be obtained in a single experiment. However, in such experiments the spatial relationship among phases that is produced by the extreme temperature gradient makes it virtually impossible to extract precise quan-titative information about phase relations and phase chemistry, especially in the near-solidus portion of the charge.

In the experiments reported on here, temperature gradients have been significantly reduced in an 18 mm

multi-anvil cell (<20°C/mm) by using stepped furnaces and highly insulating materials. Experiments are made for many hours instead of minutes, and the traditional method of making a series of isobaric experiments from subsolidus to liquidus is used to map out phase relations. The compositions of all coexisting phases in each experiment are analyzed, and phase proportions are calculated quantitatively.

Experimental techniques

Presented in Table 2 are experimental conditions and run products. Experiments at 3 GPa were made in a $\frac{1}{2}$ inch piston-cylinder device (Boyd & England, 1960) with talc–Pyrex pressure cells and ceramic spacers surrounding the sample capsule. Pressure and temperature were raised simultaneously and target experimental conditions were obtained using the 'hot piston-out' technique. On the basis of calibration of known phase transitions, a 3% correction for friction was applied, and precision in pressure is estimated to be $\pm 0{\cdot}05$ GPa. Temperatures were measured with either Type C or Type D W/Re thermocouples with no correction for the pressure effect on e.m.f., and were controlled automatically to ± 4°C.

Experiments at 4–7 GPa were made in multi-anvil devices using two types of pressure cells, both having 18 mm edge lengths: (1) cast MgO octahedra (type MA-1), and (2) pre-cast octahedra of MgO–5% Cr_2O_3 (type MA-2). The furnace assembly in both pressure cells is composed of a zirconia sleeve surrounding a stepped graphite heater with either MgO or Al_2O_3 ceramic spacers, and is identical to the high-temperature 18 mm furnace assembly described by Walter et al. (1995b), except that 7 mm o.d. zirconia sleeves were used instead of 6 mm. Experiments were made in both split-sphere and split-cylinder 6–8 type multi-anvil devices, using WC second-stage anvils with 11 mm truncated edge lengths. Pressure calibrations were made at 1200°C as described by Walter et al. (1995b), and precision in pressure is estimated to be $\pm 0{\cdot}3$ GPa. Temperatures were measured using Type C W/Re thermocouples with no correction for the pressure effect on e.m.f., and were controlled automatically to ± 3°C.

The starting material is finely crushed rock powder (10–50 μm grain size) of xenolith sample KR4003. Sample powders were contained within graphite capsules in all experiments. Octahedra, assembly parts, and the sample were fired for 1 h at 1000°C in an argon–1% hydrogen gas mixture before assembly, and after assembly were held for 6–12 h at 110–240°C before an experiment to ensure a near-anhydrous run condition. Run durations in piston-cylinder experiments ranged from 6 to 72 h, and in multi-anvil experiments from 0·5 to 24 h. In piston-cylinder runs the sample size was ~4·0 mm³, the

temperature gradient across the sample is estimated to be <10°C, and temperature reproducibility is estimated to be ± 5°C. In multi-anvil runs the sample size was ~1·0 mm³ and, on the basis of two-pyroxene thermometry (see Walter et al., 1995b), the temperature gradient across the sample is estimated at 15–25°C. Temperature reproducibility is estimated to be ± 20°C.

Analytical techniques

Presented in Tables 3–7 are analyses of coexisting phase compositions. Phases were analyzed for major and minor elements with a JEOL 8800 electron microprobe in wavelength-dispersive mode. Analytical conditions were a 15 kV accelerating potential, 10–30 nA beam current and 30 s peak acquisition time for all elements, except Na and K which were analyzed for 20 s to minimize loss by volatilization. The analytical spot size for mineral phases was 2–5 μm, and for quenched melt regions was 5–50 μm. A combination of mineral and oxide standards were used, and the minimum precision for major and minor elements is about 1% and 3% relative, respectively. The CITZAF® correction scheme was used to reduce counts to oxide concentrations. When elements are present in trace amounts (<1000 ppm), their abundances should be considered semi-quantitative.

Melt analysis

Temperature gradients, large or small, promote thermally induced compaction of melt away from solids (i.e. saturation gradient diffusion). Thermal compaction is a rapid process (see Lesher & Walker, 1988) and it is observed in both piston-cylinder and multi-anvil experiments; it cannot be eliminated as long as a temperature gradient exists and run durations are of the order of hours. However, a steady-state condition may be achieved where coexisting phase compositions represent the average equilibrium condition for the entire charge (Lesher & Walker, 1988). A benefit of this process is that pools of quenched melt (tens to hundreds of microns) tend to segregate to the hot portions of a charge, typically at the capsule walls, and the quenched melt phase is typically composed entirely of fine-grained quench crystals (microns to sub-micron). This permitted analysis of quenched melt in experiments with a minimum of ~10% melting. In some experiments there was a small amount of melting at one end or along the edges of the charge. In these, phases in contact with the melt (hot portion) were observed to have a slightly different composition from those at the cold portion of the charge (e.g. a more Mg-rich olivine in contact with the melt). A possible explanation is that, unlike experiments with higher degrees of melting, the phases at the cold end

Table 2: Experimental conditions and run products

Run no.	Cell type*	P (GPa)	T (°C)	t (h)	Phase assemblage
25.01	TP	2·5	1430	72	ol + opx + cpx + sp
26.01	TP	2·6	1415	72	ol + opx + cpx + gar + sp
30.05	TP	3	1500	66	ol + opx + cpx + gar + melt
30.12	TP	3	1515	66	ol + opx + cpx + melt
30.07	TP	3	1530	72	ol + opx + cpx + melt
30.14	TP	3	1540	48	ol + opx + melt
30.10	TP	3	1580	6	ol + opx + melt
30.11	TP	3	1630	6	ol + melt
40.02	MA-1	4	1540	24	ol + opx + cpx + gar
40.08	MA-2	4	1570	11	ol + cpx + gar + melt
40.06	MA-2	4	1590	11	ol + cpx + gar + melt
40.07	MA-2	4	1610	10	ol + opx +cpx + gar + melt
40.05	MA-1	4	1660	3	ol + opx + melt
45.07	MA-2	4·5	1580	10	ol + cpx + gar
45.03	MA-2	4·5	1620	12	ol + cpx + gar + melt
45.02	MA-2	4·5	1650	11	ol + opx + gar + melt
50.01	MA-2	5	1680	10	ol + cpx + gar + melt
60.02	MA-1	6	1670	24	ol + cpx + gar
60.04	MA-1	6	1700†	8	ol + cpx + gar + melt
60.01	MA-1	6	1710	8	ol + cpx + gar + melt
60.07	MA-2	6	1740	7	ol + cpx + ger + melt
60.05	MA-1	6	1755	6	ol + opx + cpx + gar + melt
60.03	MA-1	6	1770	6	ol + opx + melt
60.08	MA-2	6	1800	6	ol + melt
70.01	MA-1	7	1740	6	ol + cpx + gar
70.07	MA-2	7	1790	6	ol + cpx + gar + melt
70.02	MA-1	7	1810†	4	ol + cpx + gar + melt
70.05	MA-2	7	1820‡	8	ol + cpx + gar + melt
70.09	MA-2	7	1835	6	ol + opx + gar + melt
70.08	MA-2	7	1850	4	ol + gar + melt
70.06	MA-2	7	1950	1	ol + liq

*Pressure cells used in this study, where TP refers to talc–Pyrex cells used in piston-cylinder apparatus, and MA-1 and MA-2 refer to MgO and MgO–5% Cr_2O_3 cells, respectively, used in multi-anvil apparatus.
†Experimental difficulties with temperature measurement. Temperatures estimated from problematic thermocouple, furnace power, and phase assemblage.
‡Run 70.05 was made at a nominal temperature of 1780°C. A temperature of 1810°C is only an estimate made for consistency and is based on the melt composition and melt fraction.

were unable to exchange components with the melt because they were never in contact with it; that is, the solidus was spanned by the temperature gradient across the charge.

These quench features effectively eliminate the problem of phase separation of quench crystals from glass that is typical in quenched melting experiments at lower pressures (Baker & Stolper, 1994; Walter & Presnall, 1994). Even so, heterogeneous quench textures because of differential quench rates within a charge, and differential plucking of phases during polishing, pose difficulties for analyzing melts correctly. For example, in some experiments spatial heterogeneity among quench crystals occurs at a scale larger than the practical working size of the electron beam, making it difficult to reconstruct the quench composition. To minimize this problem, the beam diameter was enlarged (20–50 μm) and many spots were analyzed (typically 10–20).

Table 3: Melt compositions

Run:	30.12	30.07	30.14	30.10	30.11	40.06	40.07	40.05	45.03	45.02	50.01
n:	10	12	16	11	10	10	16	10	21	16	16
SiO_2	46.17 (21)*	46.66 (17)	46.91 (11)	48.98 (26)	47.96 (16)	46.38 (66)	45.52 (55)	46.17 (38)	45.97 (27)	46.01 (20)	44.78 (52)
TiO_2	0.91 (2)	0.70 (3)	0.64 (2)	0.48 (2)	0.39 (2)	1.45 (8)	1.27 (2)	0.46 (2)	1.66 (4)	0.49 (2)	1.26 (5)
Cr_2O_3	0.31 (2)	0.35 (1)	0.43 (2)	0.55 (3)	0.51 (5)	0.33 (2)	0.25 (2)	0.48 (5)	0.34 (2)	0.46 (2)	0.31 (1)
Al_2O_3	13.32 (14)	13.06 (16)	12.46 (9)	11.06 (25)	9.50 (9)	9.81 (22)	10.35 (19)	10.28 (22)	8.27 (11)	9.01 (21)	7.15 (13)
FeO	9.55 (18)	8.75 (18)	8.86 (16)	9.45 (21)	9.19 (12)	10.65 (59)	10.65 (48)	9.67 (22)	11.72 (34)	10.12 (16)	11.88 (38)
MgO	16.90 (19)	17.58 (35)	18.22 (11)	19.71 (71)	23.89 (56)	18.58 (64)	19.89 (30)	22.31 (41)	20.02 (36)	24.37 (66)	22.28 (33)
CaO	10.69 (14)	10.92 (14)	10.86 (8)	8.78 (27)	7.70 (22)	10.31 (30)	9.31 (16)	8.96 (14)	9.20 (17)	8.16 (23)	9.54 (20)
MnO	0.18 (1)	0.18 (1)	0.17 (1)	0.18 (1)	0.17 (1)	0.20 (2)	0.19 (1)	0.19 (1)	0.21 (1)	0.19 (2)	0.20 (1)
Na_2O	0.96 (6)	0.93 (4)	0.82 (4)	0.77 (7)	0.52 (2)	0.93 (7)	1.08 (20)	0.40 (2)	1.11 (7)	0.58 (2)	0.86 (5)
K_2O	0.56 (6)	0.41 (5)	0.34 (4)	0.23 (3)	0.22 (1)	0.83 (13)	0.70 (20)	0.22 (2)	0.99 (6)	0.29 (2)	0.60 (5)
Total	99.55 (33)	99.53 (28)	99.73 (25)	100.21 (27)	100.07 (46)	99.49 (71)	99.23 (35)	99.13 (10)	99.49 (18)	99.68 (30)	98.86 (23)
mg-no.†	75.9	78.2	78.6	78.8	82.3	75.7	76.9	80.2	75.3	81.1	77.0
Melt %‡	14	19	24	37	53	9	13	39	12	37	10

Run:	60.01	60.07	60.05	60.03	60.08	70.07	70.02	70.05	70.09	70.08	70.06
n:	10	10	22	10	8	10	10	16	12	12	8
SiO_2	44.97 (25)	45.45 (31)	46.48 (60)	46.90 (13)	47.19 (24)	45.15 (77)	46.11 (41)	47.02 (19)	47.09 (20)	47.33 (17)	45.39 (30)
TiO_2	1.01 (8)	0.91 (5)	0.49 (5)	0.36 (2)	0.30 (1)	1.23 (11)	0.66 (4)	0.58 (3)	0.43 (3)	0.28 (3)	0.21 (2)
Cr_2O_3	0.35 (2)	0.41 (2)	0.43 (2)	0.57 (2)	0.52 (3)	0.36 (2)	0.37 (4)	0.49 (1)	0.47 (3)	0.50 (2)	0.43 (3)
Al_2O_3	6.37 (10)	6.50 (11)	7.27 (32)	8.79 (16)	7.26 (16)	5.09 (16)	5.43 (17)	6.26 (10)	6.27 (4)	6.45 (15)	5.72 (42)
FeO	12.64 (35)	11.77 (23)	10.24 (32)	9.87 (12)	8.60 (7)	12.53 (62)	11.61 (31)	10.58 (15)	9.64 (10)	8.61 (12)	8.17 (24)
MgO	23.26 (35)	23.88 (25)	26.18 (64)	26.48 (22)	29.34 (39)	23.90 (63)	25.29 (54)	26.65 (28)	27.31 (18)	30.29 (39)	34.87 (1.3)
CaO	9.05 (20)	8.66 (14)	7.33 (17)	6.80 (6)	5.48 (16)	8.62 (38)	8.49 (28)	7.42 (11)	7.26 (8)	5.61 (14)	4.27 (31)
MnO	0.21 (1)	0.22 (2)	0.19 (1)	0.18 (1)	0.18 (1)	0.23 (3)	0.20 (1)	0.20 (1)	0.19 (2)	0.18 (2)	0.16 (4)
Na_2O	0.80 (2)	0.86 (3)	0.45 (2)	0.43 (1)	0.39 (2)	1.04 (4)	0.63 (3)	0.56 (1)	0.64 (4)	0.41 (2)	0.28 (3)
K_2O	0.36 (5)	0.61 (5)	0.23 (2)	0.18 (2)	0.14 (1)	0.91 (10)	0.30 (3)	0.25 (2)	0.15 (2)	0.11 (1)	0.13 (2)
Total	99.00 (16)	99.26 (16)	99.24 (12)	100.56 (25)	100.73 (6)	99.06 (24)	99.09 (13)	100.01 (12)	99.43 (18)	99.76 (17)	99.61 (35)
mg-no.	76.6	78.3	82.0	82.7	85.9	76.9	79.5	81.8	83.5	86.3	88.4
Melt %	11	19	41	50	65	16	22	35	47	66	86

* The number in parentheses in all tables is uncertainty in the least significant figures. For melts, it is two standard errors of the mean $(2\sigma/\sqrt{n})$.
† *mg*-number calculated as $(Mg/Mg + Fe) \times 100$, where $Fe^{2+}/(Fe^{2+} + Fe^{3+}) = 1$.
‡ Melt % calculated by mass balance (see text).

Table 4: Clinopyroxene compositions

Run:	30.05	30.12	30.07	40.02	40.08	40.06	40.07	45.07	45.03	50.01
n:	12	10	10	10	10	14	14	16	10	10
SiO_2	52·21 (42)*	52·47 (54)	52·06 (52)	55·40 (60)	54·08 (31)	54·38 (54)	54·27 (51)	54·43 (54)	55·14 (38)	55·10 (40)
TiO_2	0·25 (3)	0·13 (4)	0·11 (4)	0·20 (4)	0·18 (5)	0·09 (5)	0·07 (3)	0·16 (6)	0·10 (2)	0·07 (2)
Cr_2O_3	0·74 (13)	0·81 (7)	0·91 (6)	0·39 (4)	0·40 (16)	0·47 (6)	0·61 (16)	0·38 (8)	0·43 (14)	0·41 (2)
Al_2O_3	8·70 (53)	8·07 (28)	7·50 (72)	4·09 (36)	4·99 (42)	4·89 (38)	5·56 (64)	3·75 (37)	3·51 (10)	3·66 (34)
FeO	5·13 (32)	4·87 (13)	4·72 (30)	5·33 (20)	5·60 (23)	5·36 (31)	5·08 (52)	5·55 (31)	4·97 (22)	5·36 (13)
MgO	22·32 (1·0)	23·67 (62)	24·45 (1·6)	24·93 (36)	25·58 (81)	26·74 (72)	26·47 (1·0)	25·36 (88)	26·80 (68)	27·36 (94)
CaO	10·65 (1·1)	10·16 (64)	9·72 (1·8)	9·59 (46)	8·10 (78)	7·50 (58)	7·37 (50)	8·87 (88)	7·53 (64)	7·14 (76)
MnO	0·15 (3)	0·14 (3)	0·14 (3)	0·14 (2)	0·15 (3)	0·14 (3)	0·13 (2)	0·14 (2)	0·13 (2)	0·12 (2)
Na_2O	0·71 (4)	0·45 (3)	0·45 (4)	0·83 (4)	0·64 (0·07)	0·53 (3)	0·59 (16)	0·73 (10)	0·65 (8)	0·55 (3)
Total	100·86 (57)	100·77 (46)	100·06 (58)	100·90 (90)	99·72 (60)	100·10 (65)	100·15 (84)	99·37 (66)	99·26 (34)	99·77 (48)
Si	1·833	1·839	1·837	1·936	1·909	1·907	1·899	1·932	1·945	1·935
Ti	0·007	0·003	0·003	0·005	0·005	0·002	0·002	0·004	0·003	0·002
Cr	0·021	0·022	0·025	0·011	0·011	0·013	0·017	0·011	0·012	0·011
Al	0·360	0·333	0·312	0·168	0·207	0·202	0·229	0·157	0·146	0·151
Al(IV)	0·167	0·161	0·163	0·064	0·091	0·093	0·101	0·068	0·055	0·065
Al(VI)	0·193	0·172	0·149	0·105	0·116	0·108	0·128	0·089	0·091	0·087
Fe	0·151	0·143	0·139	0·156	0·165	0·157	0·149	0·165	0·147	0·157
Mg	1·168	1·237	1·286	1·299	1·346	1·398	1·380	1·342	1·409	1·432
Ca	0·401	0·382	0·368	0·359	0·306	0·282	0·276	0·337	0·285	0·269
Mn	0·004	0·004	0·004	0·004	0·004	0·004	0·004	0·004	0·004	0·004
Na	0·048	0·031	0·031	0·056	0·044	0·036	0·040	0·050	0·044	0·037
Total	3·993	3·994	4·005	3·994	3·997	4·001	3·996	4·002	3·995	3·998
mg-no.†	88·6	89·7	90·2	89·3	89·1	89·9	90·3	89·1	90·6	90·1
$K^{Fe/Mg}$‡	—	0·36	0·38	—	—	0·35	0·36	—	0·32	0·37

Run:	60.02	60.04	60.01	60.07	60.05	70.01	70.07	70.02	70.05
n:	10	10	10	10	8	12	12	16	10
SiO_2	55·65 (32)	55·96 (26)	56·18 (50)	55·91 (86)	55·84 (24)	56·06 (56)	56·23 (38)	55·82 (68)	55·95 (86)
TiO_2	0·15 (3)	0·09 (3)	0·07 (3)	0·04 (3)	0·04 (2)	0·11 (5)	0·05 (2)	0·03 (3)	0·04 (2)
Cr_2O_3	0·37 (4)	0·34 (3)	0·36 (3)	0·37 (5)	0·36 (2)	0·32 (5)	0·33 (4)	0·35 (6)	0·33 (2)
Al_2O_3	3·07 (25)	3·22 (22)	3·26 (18)	3·18 (18)	3·37 (26)	2·63 (34)	2·43 (23)	2·61 (12)	2·60 (8)
FeO	5·37 (44)	5·17 (20)	5·05 (22)	4·84 (26)	4·73 (22)	5·16 (54)	4·92 (36)	4·71 (34)	4·47 (12)
MgO	25·38 (1·4)	26·24 (72)	27·65 (1·0)	28·55 (70)	28·46 (66)	25·66 (1·5)	27·57 (1·1)	28·99 (1·0)	29·37 (66)
CaO	9·27 (1·6)	8·77 (78)	7·78 (1·3)	6·80 (58)	7·19 (64)	9·70 (1·9)	7·58 (1·4)	6·69 (88)	6·59 (74)
MnO	0·13 (2)	0·14 (3)	0·14 (3)	0·12 (4)	0·12 (2)	0·14 (3)	0·13 (2)	0·12 (2)	0·13 (2)
Na_2O	0·82 (7)	0·70 (3)	0·62 (4)	0·57 (5)	0·43 (7)	0·81 (8)	0·72 (8)	0·47 (5)	0·40 (4)
Total	100·21 (76)	100·63 (48)	101·11 (46)	100·38 (72)	100·54 (60)	100·59 (74)	99·96 (64)	99·79 (84)	99·84 (95)
Si	1·957	1·954	1·947	1·945	1·939	1·964	1·969	1·952	1·964
Ti	0·004	0·002	0·002	0·001	0·001	0·003	0·001	0·001	0·001
Cr	0·010	0·009	0·010	0·010	0·010	0·009	0·009	0·010	0·009
Al	0·127	0·132	0·133	0·130	0·138	0·109	0·100	0·107	0·106
Al(IV)	0·043	0·046	0·053	0·055	0·061	0·036	0·031	0·048	0·036
Al(VI)	0·084	0·086	0·080	0·075	0·077	0·073	0·069	0·059	0·070
Fe	0·158	0·151	0·146	0·130	0·137	0·151	0·144	0·138	0·129
Mg	1·331	1·366	1·428	1·480	1·473	1·340	1·439	1·511	1·509
Ca	0·349	0·328	0·289	0·253	0·268	0·364	0·284	0·251	0·243
Mn	0·004	0·004	0·004	0·004	0·004	0·004	0·004	0·004	0·004
Na	0·056	0·047	0·042	0·038	0·029	0·055	0·049	0·032	0·027
Total	3·996	3·993	4·001	3·991	3·999	3·999	3·999	4·006	3·992
mg-no.	89·4	90·1	90·7	91·3	91·5	89·9	90·9	91·8	92·1
$K^{Fe/Mg}$	—	—	0·34	0·34	0·42	—	0·33	0·35	0·38

* Two standard deviation uncertainty (2σ).
†mg-number = (Mg/Mg + Fe)×100, where $Fe^{2+}/(Fe^{2+} + Fe^{3+}) = 1$.
‡$K^{Fe/Mg} = (Fe_{cpx}/Fe_{melt}) \times (Mg_{melt}/Mg_{cpx})$.

Table 5: Orthopyroxene compositions

Run:	30.05	30.12	30.07	30.14	30.10	40.02	40.07	40.05	45.02	60.05	60.03	70.09
n:	12	10	10	10	7	6	6	7	7	8	7	8
SiO_2	53·28 (95)*	53·94 (70)	53·35 (70)	53·22 (80)	56·82 (48)	55·61 (1·1)	54·74 (48)	55·27 (72)	56·08 (34)	56·34 (42)	56·14 (56)	55·91 (48)
TiO_2	0·18 (6)	0·10 (2)	0·08 (3)	0·07 (4)	0·04 (2)	0·14 (3)	0·07 (3)	0·03 (2)	0·02 (2)	0·03 (2)	0·02 (1)	0·02 (2)
Cr_2O_3	0·60 (15)	0·75 (8)	0·84 (14)	0·87 (18)	0·57 (12)	0·30 (4)	0·64 (12)	0·62 (10)	0·46 (9)	0·34 (4)	0·46 (2)	0·28 (4)
Al_2O_3	8·19 (1·5)	7·25 (86)	7·05 (1·2)	5·28 (30)	3·25 (60)	3·94 (28)	5·48 (40)	4·35 (92)	3·55 (56)	3·31 (34)	3·90 (27)	2·50 (42)
FeO	6·01 (20)	5·48 (8)	5·25 (25)	5·13 (21)	4·79 (16)	6·14 (18)	5·16 (40)	4·61 (24)	4·71 (11)	4·75 (32)	3·98 (25)	4·25 (49)
MgO	30·23 (68)	30·83 (52)	31·47 (62)	31·79 (82)	34·08 (50)	32·14 (1·2)	31·47 (58)	33·13 (84)	32·93 (57)	33·19 (30)	34·23 (30)	33·82 (62)
CaO	2·29 (15)	2·49 (17)	2·45 (25)	2·56 (21)	1·37 (16)	1·93 (36)	2·42 (26)	1·66 (30)	2·20 (26)	2·25 (48)	1·48 (6)	2·02 (36)
MnO	0·13 (2)	0·12 (4)	0·12 (2)	0·13 (3)	0·10 (2)	0·12 (2)	0·11 (2)	0·11 (2)	0·11 (2)	0·11 (3)	0·09 (2)	0·09 (4)
Na_2O	0·21 (3)	0·12 (4)	0·13 (2)	0·13 (3)	0·07 (3)	0·27 (4)	0·23 (3)	0·08 (1)	0·19 (4)	0·16 (2)	0·11 (2)	0·20 (3)
Total	101·12 (52)	101·08 (34)	100·74 (48)	99·18 (49)	101·09 (46)	100·59 (1·3)	100·32 (94)	99·86 (38)	100·25 (57)	100·48 (36)	100·41 (98)	99·09 (44)
Si	1·828	1·847	1·835	1·861	1·931	1·915	1·885	1·903	1·926	1·930	1·915	1·939
Ti	0·005	0·003	0·002	0·002	0·001	0·004	0·002	0·001	0·001	0·001	0·001	0·001
Cr	0·016	0·020	0·023	0·024	0·015	0·008	0·017	0·017	0·012	0·009	0·012	0·008
Al	0·331	0·292	0·286	0·217	0·130	0·160	0·222	0·176	0·144	0·134	0·157	0·102
Al(IV)	0·172	0·153	0·165	0·139	0·069	0·085	0·115	0·097	0·074	0·070	0·085	0·061
Al(VI)	0·158	0·140	0·120	0·078	0·061	0·074	0·108	0·080	0·070	0·064	0·072	0·041
Fe	0·172	0·157	0·151	0·150	0·136	0·177	0·149	0·133	0·135	0·136	0·114	0·123
Mg	1·546	1·574	1·613	1·657	1·726	1·649	1·616	1·701	1·686	1·695	1·741	1·748
Ca	0·084	0·091	0·090	0·096	0·050	0·071	0·089	0·061	0·081	0·083	0·054	0·075
Mn	0·004	0·003	0·003	0·004	0·003	0·003	0·003	0·003	0·003	0·003	0·003	0·003
Na	0·014	0·008	0·009	0·009	0·005	0·018	0·015	0·005	0·013	0·011	0·007	0·013
Total	4·000	3·995	4·012	4·020	3·997	4·005	3·998	4·000	4·001	4·002	4·004	4·012
mg-no.†	90·0	90·9	91·4	91·7	92·7	90·3	91·6	92·8	92·6	92·6	93·9	93·4
$K^{Fe/Mg}$‡	—	0·32	0·33	0·33	0·30	—	0·31	0·32	0·34	0·37	0·31	0·36

*Two standard deviation uncertainty.
†*mg*-number $= (Mg/Mg + Fe) \times 100$, where $Fe^{2+}/(Fe^{2+} + Fe^{3+}) = 1$.
‡$K^{Fe/Mg} = (Fe_{opx}/Fe_{melt}) \times (Mg_{melt}/Mg_{opx})$.

Table 6: Garnet compositions

Run:	30.05	40.02	40.08	40.06	40.07	45.07	45.03	45.02	50.01
n:	8	8	6	8	8	6	7	8	8
SiO_2	42·42 (96)*	42·47 (20)	42·29 (32)	42·53 (21)	42·48 (50)	41·81 (70)	42·66 (30)	42·99 (20)	42·53 (34)
TiO_2	0·53 (14)	0·52 (11)	0·44 (3)	0·33 (4)	0·33 (8)	0·42 (20)	0·35 (6)	0·14 (4)	0·27 (6)
Cr_2O_3	1·53 (20)	1·32 (50)	1·26 (13)	1·40 (10)	1·66 (36)	1·12 (34)	1·01 (15)	1·82 (12)	1·40 (22)
Al_2O_3	22·20 (1·0)	22·34 (70)	22·31 (53)	22·51 (22)	22·29 (1·0)	22·12 (71)	22·47 (54)	22·24 (37)	21·91 (52)
FeO	6·22 (20)	6·45 (18)	6·03 (22)	5·61 (28)	5·46 (40)	6·29 (66)	5·46 (16)	4·64 (48)	5·76 (22)
MgO	21·81 (48)	21·99 (54)	22·54 (33)	22·89 (41)	22·98 (48)	22·59 (26)	23·38 (36)	24·41 (32)	23·54 (58)
CaO	5·43 (52)	4·71 (38)	4·69 (32)	4·65 (54)	4·85 (56)	4·67 (46)	4·27 (29)	3·47 (25)	4·11 (36)
MnO	0·20 (2)	0·20 (3)	0·18 (5)	0·17 (3)	0·17 (2)	0·18 (2)	0·19 (5)	0·16 (1)	0·17 (2)
Na_2O	0·03 (1)	0·04 (3)	0·02 (2)	0·02 (3)	0·02 (2)	0·03 (2)	0·04 (1)	0·02 (1)	0·02 (1)
Total	100·37 (36)	100·04 (78)	99·76 (90)	100·11 (55)	100·24 (60)	99·23 (22)	99·83 (38)	99·89 (60)	99·71 (67)
Si	2·986	2·994	2·984	2·985	2·980	2·971	2·994	3·002	2·996
Ti	0·028	0·028	0·023	0·017	0·017	0·022	0·018	0·007	0·014
Cr	0·085	0·073	0·070	0·078	0·092	0·063	0·056	0·100	0·078
Al	1·840	1·854	1·854	1·860	1·841	1·851	1·857	1·829	1·817
Fe	0·366	0·380	0·356	0·329	0·320	0·374	0·320	0·271	0·339
Mg	2·289	2·311	2·371	2·395	2·403	2·393	2·446	2·541	2·472
Ca	0·410	0·356	0·355	0·350	0·365	0·356	0·321	0·260	0·310
Mn	0·012	0·012	0·011	0·010	0·010	0·011	0·011	0·009	0·010
Na	0·004	0·005	0·003	0·003	0·003	0·004	0·005	0·003	0·003
Total	8·020	8·013	8·027	8·027	8·031	8·045	8·028	8·022	8·039
mg-no.†	86·2	85·9	87·0	87·9	88·2	86·5	88·4	90·4	87·9
$K^{Fe/Mg}$‡	—	—	—	0·43	0·44	—	0·40	0·46	0·46

Table 6: continued

Run:	60-02	60-04	60-01	60-07	60-05	70-01	70-07	70-02	70-05	70-09	70-08
n:	10	8	8	8	8	8	8	8	10	10	8
SiO_2	42·15 (54)	42·89 (30)	43·41 (68)	43·44 (21)	42·83 (46)	42·88 (56)	43·91 (28)	43·30 (30)	43·89 (32)	43·57 (45)	44·32 (32)
TiO_2	0·55 (5)	0·40 (13)	0·35 (11)	0·26 (14)	0·18 (8)	0·51 (7)	0·33 (12)	0·17 (4)	0·28 (5)	0·11 (4)	0·09 (5)
Cr_2O_3	1·71 (38)	1·01 (22)	1·39 (44)	1·26 (28)	1·28 (64)	1·54 (36)	1·21 (64)	1·44 (26)	1·04 (30)	1·43 (21)	1·36 (9)
Al_2O_3	21·68 (36)	21·98 (35)	21·96 (68)	21·96 (20)	22·11 (26)	20·93 (32)	21·14 (78)	21·22 (26)	21·65 (46)	21·36 (50)	21·19 (16)
FeO	6·52 (26)	5·83 (31)	5·80 (40)	5·10 (22)	4·83 (24)	6·37 (30)	5·43 (21)	4·88 (28)	4·55 (78)	4·20 (13)	3·70 (14)
MgO	22·40 (46)	22·96 (36)	23·36 (32)	24·22 (26)	24·23 (60)	23·14 (40)	24·21 (84)	24·69 (32)	24·44 (96)	25·80 (90)	26·73 (32)
CaO	4·44 (16)	4·58 (46)	4·04 (80)	3·88 (20)	3·90 (36)	4·30 (26)	4·00 (48)	3·64 (14)	3·85 (84)	2·98 (31)	2·24 (14)
MnO	0·19 (2)	0·18 (3)	0·17 (3)	0·16 (3)	0·15 (3)	0·19 (4)	0·16 (3)	0·15 (2)	0·16 (3)	0·12 (4)	0·12 (3)
Na_2O	0·04 (2)	0·04 (2)	0·02 (1)	0·03 (1)	0·02 (1)	0·05 (2)	0·04 (2)	0·03 (2)	0·03 (1)	0·03 (2)	0·02 (1)
Total	99·68 (68)	99·87 (90)	100·50 (60)	100·31 (23)	99·53 (81)	99·91 (62)	100·43 (68)	99·52 (30)	99·89 (1·2)	99·60 (42)	99·77 (28)
Si	2·987	3·016	3·029	3·025	3·005	3·026	3·059	3·038	3·058	3·038	3·068
Ti	0·029	0·021	0·018	0·014	0·009	0·027	0·017	0·009	0·015	0·006	0·005
Cr	0·096	0·056	0·077	0·069	0·071	0·086	0·067	0·080	0·057	0·079	0·074
Al	1·809	1·820	1·804	1·801	1·826	1·739	1·734	1·753	1·776	1·754	1·728
Fe	0·386	0·343	0·338	0·297	0·283	0·376	0·316	0·286	0·265	0·245	0·214
Mg	2·367	2·407	2·429	2·514	2·534	2·435	2·514	2·582	2·538	2·682	2·759
Ca	0·337	0·345	0·302	0·290	0·293	0·325	0·299	0·274	0·287	0·223	0·166
Mn	0·011	0·011	0·010	0·009	0·009	0·011	0·009	0·009	0·009	0·007	0·007
Na	0·005	0·005	0·003	0·004	0·003	0·007	0·005	0·004	0·004	0·004	0·003
Total	8·027	8·024	8·010	8·023	8·033	8·032	8·020	8·035	8·009	8·038	8·024
mg-no.	86·0	87·3	87·8	89·4	89·9	86·6	88·8	90·0	90·6	91·6	92·8
$K^{Fe/Mg}$	—	—	0·46	0·43	0·51	—	0·42	0·43	0·47	0·46	0·49

*Two standard deviation uncertainty.
†mg-number = (Mg/Mg + Fe) × 100, where $Fe^{2+}/(Fe^{2+} + Fe^{3+}) = 1$.
‡$K^{Fe/Mg} = (Fe_{gar}/Fe_{melt}) \times (Mg_{melt}/Mg_{gar})$.

Table 7: Olivine compositions

Run:	30.05	30.12	30.07	30.14	30.10	30.11	40.02	40.08	40.06	40.07	40.05	45.07	45.03	45.02	50.01
n:	10	10	10	8	8	8	10	8	10	8	10	10	10	8	8
SiO_2	40.24 (88)*	40.36 (29)	40.14 (20)	40.03 (29)	40.90 (14)	40.96 (26)	40.30 (23)	40.17 (30)	40.37 (30)	40.30 (26)	40.44 (18)	39.38 (50)	40.09 (20)	40.39 (30)	40.40 (56)
Cr_2O_3	0.14 (3)	0.19 (3)	0.22 (3)	0.24 (3)	0.27 (2)	0.27 (3)	0.08 (2)	0.10 (3)	0.13 (3)	0.14 (3)	0.22 (4)	0.12 (3)	0.15 (3)	0.21 (3)	0.12 (2)
Al_2O_3	0.21 (5)	0.23 (5)	0.22 (3)	0.22 (8)	0.18 (1)	0.19 (2)	0.13 (3)	0.15 (3)	0.23 (3)	0.21 (3)	0.21 (2)	0.18 (5)	0.20 (6)	0.24 (2)	0.22 (3)
FeO	10.23 (16)	9.33 (7)	8.74 (13)	8.61 (16)	7.79 (10)	7.02 (14)	10.32 (20)	10.08 (34)	9.44 (25)	9.48 (25)	7.61 (8)	10.69 (38)	9.05 (52)	7.57 (28)	9.23 (8)
MgO	49.45 (34)	50.02 (42)	49.97 (34)	49.80 (90)	51.23 (38)	51.99 (13)	49.04 (22)	49.01 (26)	49.79 (28)	49.59 (66)	50.76 (36)	48.50 (86)	49.71 (66)	50.96 (70)	49.52 (25)
CaO	0.25 (2)	0.28 (4)	0.25 (2)	0.35 (6)	0.20 (2)	0.20 (2)	0.21 (2)	0.28 (3)	0.30 (3)	0.30 (3)	0.21 (2)	0.28 (4)	0.30 (8)	0.26 (2)	0.30 (4)
MnO	0.13 (3)	0.13 (3)	0.13 (3)	0.13 (3)	0.11 (3)	0.09 (3)	0.13 (3)	0.12 (3)	0.13 (3)	0.12 (2)	0.11 (2)	0.13 (2)	0.13 (2)	0.11 (4)	0.14 (3)
Total	100.65 (95)	100.54 (38)	99.67 (36)	99.38 (94)	100.68 (29)	100.72 (32)	100.21 (19)	99.91 (46)	100.39 (40)	100.14 (98)	99.56 (48)	99.28 (94)	99.63 (30)	99.74 (61)	99.93 (54)
Si	0.983	0.983	0.984	0.984	0.987	0.985	0.988	0.988	0.985	0.986	0.987	0.978	0.985	0.984	0.989
Cr	0.003	0.004	0.004	0.005	0.005	0.005	0.002	0.002	0.003	0.003	0.004	0.002	0.003	0.004	0.002
Al	0.006	0.007	0.006	0.006	0.005	0.005	0.004	0.004	0.007	0.006	0.006	0.005	0.006	0.007	0.006
Fe	0.209	0.190	0.179	0.177	0.157	0.141	0.212	0.207	0.193	0.194	0.155	0.222	0.186	0.154	0.189
Mg	1.801	1.817	1.826	1.825	1.843	1.865	1.792	1.796	1.812	1.809	1.847	1.796	1.820	1.851	1.808
Ca	0.007	0.007	0.007	0.009	0.005	0.005	0.006	0.007	0.008	0.008	0.005	0.007	0.008	0.007	0.008
Mn	0.003	0.003	0.003	0.003	0.002	0.002	0.003	0.002	0.003	0.002	0.002	0.003	0.003	0.002	0.003
Total	3.012	3.011	3.009	3.009	3.004	3.008	3.007	3.006	3.001	3.008	3.006	3.013	3.011	3.009	3.005
mg-no.†	89.6	90.5	91.1	91.2	92.1	93.0	89.4	89.7	90.4	90.3	92.2	89.0	90.7	92.4	90.5
$K^{Fe/Mg}$‡	—	0.33	0.35	0.36	0.32	0.35	—	—	0.33	0.36	0.35	-	0.31	0.36	0.35

Run:	60.02	60.04	60.01	60.07	60.05	60.03	60.08	70.01	70.07	70.02	70.05	70.09	70.08	70.06
n:	10	10	10	10	10	10	8	10	10	10	10	8	10	8
SiO_2	40.79 (38)	40.18 (23)	40.61 (44)	40.53 (21)	40.47 (44)	41.16 (26)	40.99 (14)	40.23 (12)	40.44 (56)	40.52 (42)	40.52 (18)	40.32 (46)	40.87 (27)	40.72 (30)
Cr_2O_3	0.09 (2)	0.14 (2)	0.13 (2)	0.17 (3)	0.18 (3)	0.21 (3)	0.18 (3)	0.09 (2)	0.13 (3)	0.14 (3)	0.17 (3)	0.18 (3)	0.19 (3)	0.16 (4)
Al_2O_3	0.14 (6)	0.18 (2)	0.22 (3)	0.20 (3)	0.24 (2)	0.27 (2)	0.19 (3)	0.14 (4)	0.17 (4)	0.23 (3)	0.23 (3)	0.17 (3)	0.25 (3)	0.23 (4)
FeO	10.28 (34)	9.80 (18)	9.19 (12)	8.53 (11)	7.28 (50)	6.82 (40)	5.52 (10)	10.0 (18)	8.63 (21)	8.45 (18)	7.40 (7)	6.51 (13)	5.28 (34)	4.59 (26)
MgO	48.97 (35)	49.10 (36)	50.12 (30)	50.56 (74)	51.13 (42)	51.79 (58)	52.91 (51)	48.94 (62)	50.41 (48)	50.26 (74)	50.99 (17)	51.98 (22)	52.55 (64)	53.41 (68)
CaO	0.20 (5)	0.25 (2)	0.24 (2)	0.29 (3)	0.20 (3)	0.16 (2)	0.16 (2)	0.21 (5)	0.26 (3)	0.23 (4)	0.21 (1)	0.22 (2)	0.18 (2)	0.13 (2)
MnO	0.13 (3)	0.13 (2)	0.13 (2)	0.11 (2)	0.10 (3)	0.09 (2)	0.09 (2)	0.12 (2)	0.12 (2)	0.12 (2)	0.11 (2)	0.09 (2)	0.08 (2)	0.07 (2)
Total	100.60 (66)	99.78 (62)	100.64 (70)	100.39 (72)	99.60 (56)	100.50 (84)	100.04 (52)	99.73 (66)	100.16 (64)	99.95 (86)	99.63 (35)	99.47 (46)	99.40 (70)	99.31 (72)
Si	0.995	0.988	0.987	0.985	0.985	0.990	0.986	0.990	0.986	0.988	0.987	0.981	0.988	0.983
Cr	0.002	0.003	0.002	0.003	0.003	0.004	0.003	0.002	0.003	0.003	0.003	0.003	0.004	0.003
Al	0.004	0.005	0.006	0.006	0.007	0.008	0.005	0.004	0.005	0.007	0.007	0.005	0.007	0.007
Fe	0.210	0.201	0.187	0.173	0.148	0.137	0.111	0.206	0.176	0.172	0.151	0.132	0.107	0.093
Mg	1.780	1.799	1.816	1.832	1.856	1.858	1.897	1.795	1.832	1.827	1.852	1.885	1.894	1.922
Ca	0.005	0.007	0.006	0.008	0.005	0.004	0.004	0.006	0.007	0.006	0.005	0.006	0.005	0.003
Mn	0.003	0.003	0.003	0.002	0.002	0.002	0.002	0.003	0.002	0.002	0.002	0.002	0.002	0.001
Total	2.999	3.006	3.007	3.009	2.999	3.003	3.008	3.006	3.011	3.005	3.007	3.014	3.007	3.012
mg-no.	89.5	88.9	90.7	91.5	92.6	93.0	94.5	89.7	91.2	91.4	92.5	93.4	94.7	95.4
$K^{Fe/Mg}$	—	—	0.34	0.34	0.36	0.36	0.36	-	0.32	0.37	0.37	0.35	0.35	0.37

*Two standard deviation uncertainty.
†*mg*-number = (Mg/Mg + Fe) × 100, where $Fe^{2+}/(Fe^{2+} + Fe^{3+}) = 1$.
‡$K^{Fe/Mg} = (Fe_{ol}/Fe_{melt}) \times (Mg_{melt}/Mg_{ol})$.

The quenched melts in two experiments were particularly difficult to analyze. In one, run 30.10, the quenched melt was homogeneously distributed throughout the charge, and no quench regions larger than ~10 μm were available for analyses. In these melt regions, the quench crystals were large and of variable composition. The odd composition of this melt with respect to others at 3 GPa (e.g. high SiO_2) suggests that the actual melt composition was not attainable. In the second, run 40.05, the melt quenched as a large pool, but was a mixture of glass and quench crystals. The melt composition given in Table 3 was reconstructed from analyses of both quench and glass, in proportions reflecting their perceived abundances in the melt pool.

Modal calculations

To discuss phase relations quantitatively, the modal proportions of phases in each experiment must be known. Modal proportions (wt %) are calculated by mass balance between the compositions of coexisting phases and the system bulk composition. This is done by solving for $\boldsymbol{x}$ in the matrix equation, $\boldsymbol{A} \cdot \boldsymbol{x} = \boldsymbol{b}$, where $\boldsymbol{A}$ is an $M \times \mathcal{N}$ matrix composed of M phases and $\mathcal{N}$ components (composition matrix), $\boldsymbol{x}$ is the solution vector (phase modes) and $\boldsymbol{b}$ is a known vector (bulk composition). Because there are ten major and minor element components, systems with two to five phases are overdetermined. To circumvent this problem, only the major element components SiO_2, Al_2O_3, FeO, MgO and CaO are used to mass balance experiments with three to five phases, and SiO_2, FeO and MgO are used in experiments with two to three phases. In most cases the set of equations is still overdetermined, but robust solutions, in the least-squares sense, can be obtained for such systems. A singular value decomposition method (Press *et al.*, 1992) was used to solve the mass-balance equations. To assess the uncertainties in the calculated modes that are associated with microprobe analytic uncertainty, Monte Carlo simulations were performed. Microprobe error (2σ for solid phases and $2\sigma/\sqrt{n}$ for melt) was randomly distributed about the average composition for each oxide in each phase, and 400 solutions to the matrix equation were generated. The resultant modes were then treated statistically. Presented in Table 8 are the calculated modal proportions of phases for each experiment with one standard variance uncertainty. For nearly all experiments, the calculated modes reproduced the observed phase assemblages. The exceptions are runs 70.08 and 60.05. A negative coefficient was obtained for garnet ($-1\cdot0$ wt %) in run 70.08 and for clinopyroxene (cpx: $-1\cdot6$ wt %) in run 60.05. These phases are present in minor amounts in these experiments, indicating that they were nearly consumed in the melt. It is likely that when the temperature gradient in an experiment is close to or spans

a phase boundary, compositional variations owing to the temperature gradient overwhelm the resolution of the modal calculations.

Attainment of equilibrium

The experiments reported here have not been reversed so equilibrium cannot be proved rigorously. However, data from liquidus experiments reported by Presnall *et al.* (1978) show that phase boundary reversals based on appearance and disappearance of phases require less time than that required for homogenization of phase compositions, and are on the order of 2–4 h for peridotite phases crystallized from melt at 1400–1600°C. Nearly all experiments reported here, with the exception of near-liquidus experiments, are at least a factor of two longer in duration than this minimum, and most are at higher temperatures, which should facilitate more rapid equilibration.

Phase homogeneity

A more rigorous assessment of equilibrium can be made from observations of phase homogeneity, and by considering exchange equilibria between melts and solids. At equilibrium, the observed uncertainties in phase compositions within a single experiment should be within the microprobe analytic uncertainty.

Melt. Uncertainties in melt composition are given as two standard errors of the mean ($2\sigma/\sqrt{n}$) in Table 3. This statistical measure is appropriate when analyzing complex mixtures of quench phases wherein much of the uncertainty can be attributed to random sampling by the probe beam rather than inherent heterogeneity. On average, uncertainties for most elements in all melts are ~1% relative, very near microprobe uncertainty levels and indicating homogeneity. Among major elements, Mg and Fe exhibit the most variation with average uncertainties of ~2% relative. Na and K uncertainties are typically 5–10% relative, but can be as high as 20% in low-degree melts. This feature is puzzling, but may be attributable to Na- and K-rich quench segregations that are interstitial to other quench crystals and polish differentially. There is no indication of melt heterogeneity caused by chemical diffusion in the temperature gradient (Soret effect).

Olivine. At the two standard deviation level (2σ), uncertainties for Si, Fe and Mg are typically 1–2% relative, somewhat larger than microprobe uncertainty. Fe–Mg exchange between mineral and melt, calculated as $K_D = (Fe_{min}/Fe_{melt}) \times (Mg_{melt}/Mg_{min})$, gives a value of $0\cdot35 \pm 3$ (2σ, where error is assigned to the least significant digit).

Pyroxenes. At the 2σ level, all major elements in pyroxenes exhibit variations greater than expected from

Table 8: Modal abundances of phases (in weight percent)

Exp. no.	Olivine	Opx	Cpx	Garnet	Melt	ΣR^{2*}
30.05	53·1 (9)†	17·7 (2·5)	27·3 (1·8)	1·9 (9)	trace‡	0·53
30.12	52·5 (5)	19·8 (1·0)	14·0 (1·6	—	13·8 (1·1)	0·39
30.07	51·5 (6)	20·6 (2·1)	9·4 (2·7)	—	18·5 (1·4)	0·59
30.14	50·5 (9)	25·1 (9)	—	—	24·4 (3)	0·40
30.10	52·9 (5)	9·9 (8)	—	—	37·2 (8)	0·29
30.11	47·3 (5)	—	—	—	52·7 (3)	1·58
40.02	53·6 (4)	5·6 (1·2)	27·9 (9)	12·9 (3)	—	0·36
40.08	53·3 (5)	—	35·7 (5)	11·0 (4)	trace	0·46
40.06	52·3 (5)	—	30·5 (9)	8·0 (5)	9·2 (1·0)	0·32
40.07	51·5 (8)	7·1 (2·5)	23·3 (2·8)	5·2 (7)	12·9 (1·7)	0·30
40.05	47·0 (4)	14·2 (8)	—	—	38·8 (8)	0·53
45.07	53·0 (8)	—	34·0 (7)	13·0 (4)	—	0·33
45.03	51·8 (6)	—	25·8 (1·2)	10·2 (4)	12·2 (1·6)	0·26
45.02	44·0 (6)	17·8 (7)	—	1·0 (4)	37·2 (7)	0·34
50.01	50·6 (5)	—	28·3 (7)	11·1 (3)	10·0 (7)	0·40
60.02	54·8 (7)	—	30·0 (7)	15·2 (3)	—	0·23
60.04	53·4 (4)	—	31·9 (4)	14·7 (3)	trace	0·73
60.01	50·3 (5)	—	26·6 (6)	12·1 (3)	11·0 (9)	0·36
60.07	47·8 (6)	—	22·6 (6)	10·2 (2)	19·4 (6)	0·28
60.05	41·8 (8)	15·4 (2·1)	−1·6 (2·8)	3·3 (7)	41·1 (2·3)	0·36
60.03	41·6 (5)	8·7 (1·2)	—	—	49·7 (7)	0·41
60.08	35·0 (5)	—	—	—	65·0 (4)	0·64
70.01	53·8 (8)	—	29·6 (7)	16·7 (4)	—	0·42
70.07	48·5 (6)	—	22·1 (8)	13·7 (4)	15·7 (1·0)	0·22
70.02	46·7 (6)	—	19·8 (7)	11·8 (2)	21·7 (8)	0·31
70.05	44·4 (4)	—	12·7 (5)	7·8 (2)	35·1 (7)	0·38
70.09	39·5 (3)	8·4 (5)	—	4·7 (2)	47·4 (5)	0·56
70.08	32·9 (6)	—	—	−1·0 (3)	68·1 (7)	0·81
70.06	13·8 (2·1)	—	—	—	86·2 (1·8)	0·81

*Sum of the square of the residuals calculated by solving for **b** in **A·x** = **b** using phase proportions (**A**) and phase compositions (**x**, normalized to 100%) for all elements, and finding the absolute difference (residuals) from the bulk composition, KR4003.
†One standard variance uncertainty from microprobe error as calculated from Monte Carlo simulation (see text).
‡Trace refers to an estimate of <5% melting. Mode calculated on a melt-free basis.

microprobe uncertainty. Average relative errors are ~2% for Si, 3% for Fe, 4% for Mg, and 10% for Ca and Al. Clinopyroxenes and orthopyroxenes have K_D values of 0·35 ± 5 and 0·33 ± 4, respectively.

Garnet. In subsolidus and near-solidus runs, the presence of aluminous spinel in the cores of some garnet grains precludes complete equilibration. These grains were avoided during analysis. For major elements, average relative errors are ~1% for Si, ~3% for Fe, Mg and Al, and ~5% for Ca. Garnets have an average K_D of 0·45 ± 6. Average errors in the minor elements Cr and Ti are ~15% relative.

Element uncertainties in solid phases are typically greater than microprobe analytic uncertainty, indicating that the experiments have not reached complete equilibrium with respect to all exchange components. However, circumstantial evidence for a close approach to equilibration is that observed K_D values for all phases are relatively constant and are consistent with observations from other peridotite melting experiments. For example, Herzberg & Zhang (1996) reported an average olivine–melt K_D of 0·33 ± 6 and a garnet–melt K_D of about 0·48 ± 6 in high-pressure melting experiments on KLB-1, whereas Agee *et al.* (1995) reported an olivine–melt K_D of 0·36 ± 9 for melting of Allende chondrite at 10 GPa. Kinzler (1997) has reported K_D values of 0·33 ± 3 for olivine, 0·36 ± 4 for cpx, 0·33 ± 4 for opx and 0·54 ± 6 for garnet in peridotite melting experiments

at 1·5–2·3 GPa, and found that typically $K_D$gar > $K_D$cpx > $K_D$ol > $K_D$opx. The absolute K_D values from these experiments, and their values relative to each other, are generally consistent with those in the experiments reported on here.

Finally, the modal abundances of phases in each experiment, as determined by mass balance, show that mass is conserved within a reasonable degree of uncertainty in all experiments (Table 8).

Phase relations

Figure 1 is a pressure–temperature isopleth for composition KR4003. For clarity, the only phase boundaries drawn in the diagram are those showing the position of the subsolidus transition from spinel to garnet lherzolite, the solidus, and an outline of the supra-solidus region within which orthopyroxene (opx) is stable. The transition from spinel to garnet lherzolite at the solidus is estimated to occur at ~2·6 GPa and 1450°C, although in detail this transition will occur over a range of pressure and temperature. The temperature range of opx stability is reduced with increase in pressure and, although the data extend only to 7 GPa, indications are that opx will no longer be present in the melting interval above ~10 GPa, generally consistent with the results of Zhang & Herzberg (1994) for KLB-1. Canil (1992), who also made experiments in a cell with a relatively low temperature gradient, and Takahashi (1986) both determined a solidus temperature for peridotite KLB-1 of ~1625°C at 5 GPa, which is very close to the solidus of KR4003 at this pressure (~1640°C). However, Takahashi *et al.* (1993) and Zhang & Herzberg (1994) located the solidus of KLB-1 at ~1725°C at 5 GPa. Some of these differences may be explained by interlaboratory pressure and temperature biases, although the solidus of KR4003 might be somewhat lower than that of KLB-1 because KR4003 is more fertile, having lower MgO, and higher SiO_2 and Al_2O_3 contents.

Figure 2 is a pressure–percent melting isopleth that is constructed on the basis of modal calculations. Takahashi (1986) and Takahashi *et al.* (1993) reported that opx was not stable at the solidus or in the melting interval of peridotite KLB-1 above a pressure of ~3·5 GPa. Conversely, Herzberg *et al.* (1990), Canil (1992) and Zhang & Herzberg (1994) reported opx in the melting interval of KLB-1 up to pressures of ~10 GPa. In agreement with Takahashi (1986) and Takahashi *et al.* (1993), between 2·6 and 3·3 GPa, the solidus assemblage for KR4003 is olivine + opx + cpx + garnet + melt, but above 3·3 GPa opx is no longer stable at the solidus, and the assemblage is olivine + cpx + garnet + melt. However, in agreement with Herzberg *et al.* (1990), Canil (1992) and Zhang & Herzberg (1994), above 3·3 GPa opx

crystallizes from melt at temperatures above the solidus.

The change from a two-pyroxene to a single-pyroxene assemblage at 3·3 GPa occurs because the enstatite component of cpx at the solidus increases continuously with pressure and temperature, and eventually pyrolitic compositions lie outside the composition space defined by the assemblage olivine + opx + cpx + garnet (see also Kinzler & Grove, 1992a; Bertka & Holloway, 1993; Walter *et al.*, 1995a; Longhi & Bertka, 1996). Heating above the solidus causes opx to crystallize from the melt by incongruent melting of cpx to form opx + melt. This generates the peritectic reactions, olivine + cpx + garnet = melt + opx and ol + cpx = opx + melt. Peritectic melting of peridotite at high pressures, with opx crystallizing from melt upon heating, has been identified previously (e.g. Davis, 1964; O'Hara & Yoder, 1967; Mysen & Kushiro, 1977; Herzberg *et al.*, 1990; Bertka & Holloway, 1993; Walter *et al.*, 1995a). Below 3·3 GPa peritectic melting begins at the solidus, but at pressures above 3·3 GPa the degree of melting at which opx crystallizes from melt increases with pressure; for example, at 4 GPa the peritectic reaction begins at ~12% melting, and at 7 GPa at ~38% melting. Although opx crystallizes upon heating above the solidus, it is eventually dissolved back into the melt. The first phase to be consumed during melting changes from garnet at pressures below ~4·2 GPa to cpx at higher pressure, and garnet stability continues to increase to higher degrees of melting with increase in pressure. Indeed, garnet is stable to higher degrees of melting than opx at pressures above ~6·6 GPa.

Takahashi *et al.* (1993) made a number of experiments between the solidus and liquidus of KLB-1 at both 4·6 and 6·5 GPa using an assembly with a low temperature gradient, but never observed opx in the melting interval. This is at odds with data for melting of KR4003, but more disturbingly, is at odds with results from other laboratories for melting of KLB-1. However, Fig. 2 provides a means of reconciliation between these apparently discrepant results. At 4·6 GPa, Takahashi *et al.* have a gap in their experiments between 22 and 55% melting, and at 6·5 GPa a gap exists between 34 and 72% melting. Figure 2 shows that these gaps correspond closely to the range of melting where opx is stable at these pressures. Perhaps an unfortunate spacing of experiments in the study by Takahashi *et al.* precluded their observing opx in the melting interval.

Melting reactions

Shown in Fig. 3 are modal abundances of residual minerals as a function of melt percent at 3 and 7 GPa. These curves are constructed on the basis of the modal abundances given in Table 8, and curves are drawn to
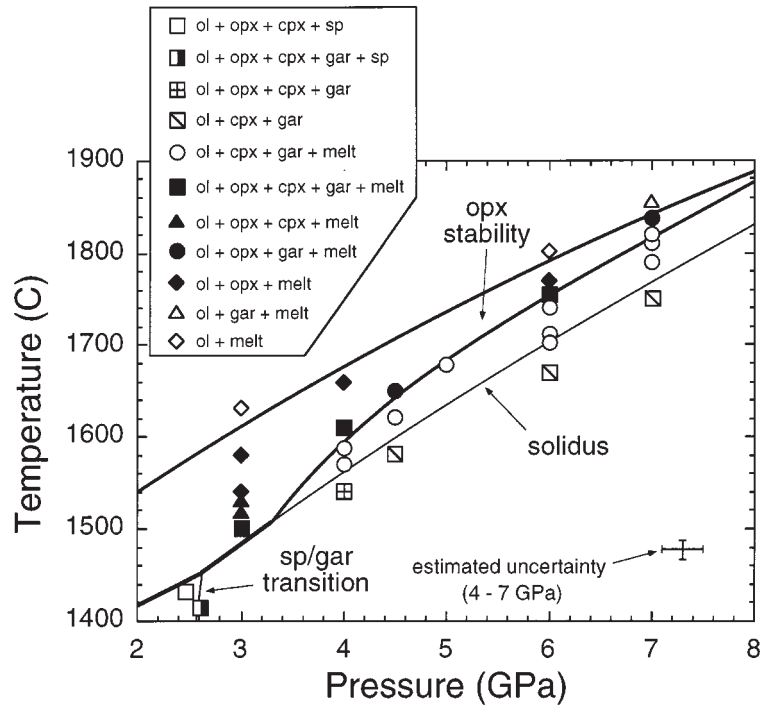
Fig. 1. Pressure–temperature isopleth for equilibrium melting of peridotite KR4003. Run conditions are given in Table 1. Abbreviations in all figures: ol, olivine; opx, orthopyroxene; cpx, clinopyroxene; gar, garnet; sp, spinel. Filled symbols denote an assemblage containing opx. Contours show the solidus, the field of opx stability (bold lines), and the spinel to garnet lherzolite subsolidus transition. Opx is not stable at the solidus above 3·3 GPa, but crystallizes from melt above the solidus.
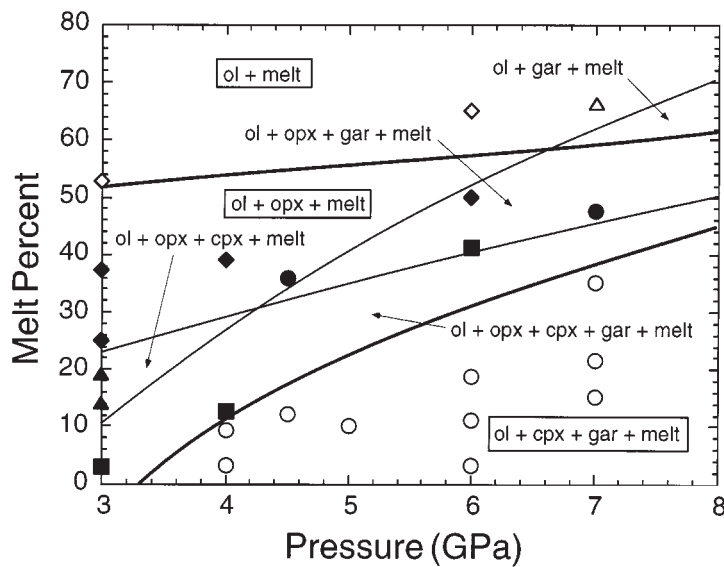

Fig. 2. Pressure–melt percent (wt %) isopleth for KR4003, based on the modal calculations given in Table 8. Symbols are as in Fig. 1. Bold lines show the field of opx stability.

be consistent with the phase boundaries in Fig. 2. Changes in modal abundances can be used to calculate melting reactions using the method of Walter *et al.* (1995*a*).

Table 9 gives melting reactions over discrete melting intervals corresponding in most cases to the appearance and disappearance of phases. These reactions give the

Table 9: Garnet peridotite melting reactions at 3 and 7 GPa (in weight units)

Melting interval	Reaction
3 GPa	
0–10% (garnet-out)	7 olivine + 68 cpx + 25 garnet = 84 melt + 16 opx
10–23% (cpx-out; opx-max.)	6 olivine + 94 cpx = 64 melt + 36 opx
23–50% (opx-out)	3 olivine + 97 opx = 100 melt
7 GPa	
0–10%	26 olivine + 50 cpx + 24 garnet = 100 melt
10–38% (opx-in)	25 olivine + 51 cpx + 24 garnet = 100 melt
38–46% (cpx-out; opx-max.)	18 olivine + 57 cpx + 25 garnet = 46 melt + 54 opx
46–60% (opx-out)	13 olivine + 62 opx + 25 garnet = 100 melt
60–65% (garnet-out)	68 olivine + 32 garnet = 100 melt
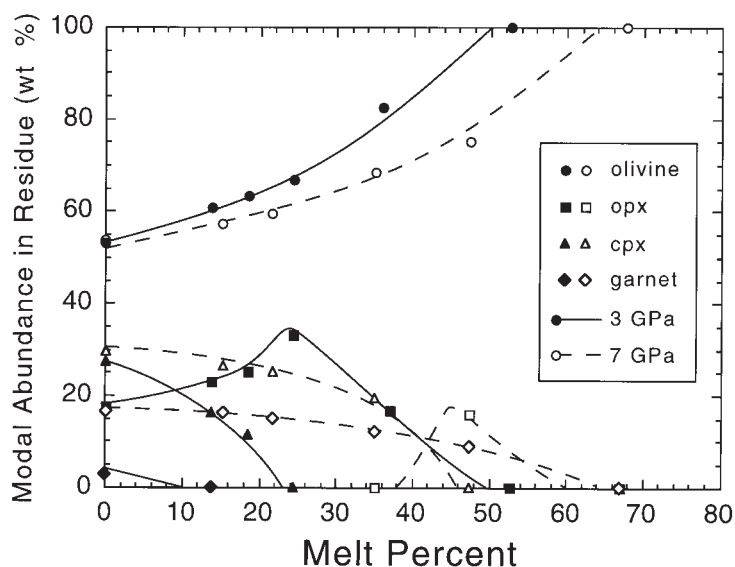
Fig. 3. Modal abundance of phases in the residue (normalized to 100 wt % solids) vs percent melting (wt %). Curves are fitted to the data by eye. Filled and open symbols are for 3 and 7 GPa data points, respectively. Melting reactions in Table 9 are calculated on the basis of these curves.

net change in mass of phases over large melting intervals. Conversely, an instantaneous reaction calculated over an infinitely small melting interval will have a different stoichiometry. However, these reactions provide a general basis for discussing the relative contributions of phases to melting.

The solidus melting reaction at 3 GPa is of peritectic type, and opx crystallizes from melt during heating. Opx abundance in the residue (Fig. 3) reaches a maximum when cpx is completely dissolved in the melt, and further heating dissolves opx and olivine. At 7 GPa, opx is not present at the solidus, and the melting reaction is of eutectic type. At ~38% melting, opx begins to crystallize from melt during heating and reaches a maximum in the residue at ~46% melting, again corresponding to elimination of cpx in the residue. Continued heating dissolves prodigious amounts of opx into the melt, and causes an increase in SiO_2. The phase relations of the pyroxenes at the peridotite solidus, and throughout the melting interval, are explicable in terms of the topological treatment of phase relations along the En–Di join suggested by Longhi & Bertka (1996); specifically, the data

for KR4003 are consistent with the topology depicted in their fig. 3b. Further, Milholland & Presnall (1998) have deduced very similar phase relations for melting of garnet lherzolite in the system CaO–MgO–Al_2O_3–SiO_2 (CMAS) at 3 GPa.

Melt compositions

Plotted in Fig. 4 are melt compositions from Table 3 as projected from cpx onto olivine–opx–garnet using the garnet lherzolite normative scheme of Kelemen *et al.* (1992). Isobaric equilibrium melting trends are distinctly defined on this projection and, although a single normative projection cannot convey all compositional features, the general phase relations of melting are adequately portrayed. Shown as a dashed line is the approximate position of the opx-in curve, meaning that opx is present to the opx-rich side of the curve. The opx-in curve effectively defines the trend of melts in equilibrium with four-phase garnet lherzolite as a function of pressure. Shown as a bold continuous line is the garnet-out curve, meaning that garnet is not present to the opx-rich side of the curve. During isobaric melting, low-degree melts of less than ~10% do not contain normative opx (nepheline normative in the CIPW scheme) over the experimental pressure range. Thus, initial melts on the fertile garnet peridotite solidus do not become enstatite normative with increase in pressure, in apparent contradiction to the predictions of O'Hara (1968) and Walter & Presnall (1994) based on data from simplified systems (but see below). With increased isobaric heating, melts become progressively enriched in normative opx and garnet relative to olivine, until the garnet-out curve is reached. At this point, continued heating moves melt compositions toward opx until opx exhaustion in the residue, after which melts move toward the bulk composition as olivine dissolves into the melt. At constant degree of melting, melt compositions move in the general direction of normative olivine with increase in pressure, because of expansion and contraction of the garnet and olivine stability fields, respectively (see also Herzberg, 1992). For comparison, shown in Fig. 4b are data for isobaric invariant melting of garnet lherzolite at 3–10 GPa in the system CaO–MgO–Al_2O_3–SiO_2 (CMAS) from the work of Gudfinnsson & Presnall (1996) and Herzberg & Zhang (1997, submitted). The trend for isobaric melting in CMAS is remarkably consistent with the trend of the opx-in curve for KR4003, although CMAS melts are displaced to higher garnet contents at a given pressure. Solidus melts in the CMAS system in equilibrium with four-phase garnet lherzolite become more opx-rich with pressure, vindicating the predictions mentioned above. However, at the solidus of fertile natural peridotite, opx is not stable above ~3·3 GPa and solidus melts are opx deficient.

Figure 5 shows oxide vs degree of melting plots for major and minor elements. Polynomial curves have been fitted to the major element data and Cr_2O_3, and power-law curves to the incompatible minor elements. These curves do not have functional forms that can adequately recapture the complex chemical variations in all cases. Indeed, the data are not always sufficiently precise to render meaningful parameterizations. Instead, these curves are used as visual guides for deducing generalized trends. For major elements the competing effects of pressure and degree of melting are clearest for MgO, CaO and Al_2O_3. At constant pressure, MgO increases and CaO decreases with melting, whereas Al_2O_3 increases to a maximum corresponding to garnet exhaustion in the residue and then decreases. At constant degree of melting, MgO increases with pressure and CaO and Al_2O_3 decrease with pressure. Similar to Al_2O_3, both SiO_2 and Cr_2O_3 apparently increase to a maximum and then decrease with increased melting. Maxima in SiO_2 can be attributed to opx exhaustion in the residue. There is a strong indication that SiO_2 decreases with increase in pressure at constant degree of melting, but uncertainties are too large to be sure of this. FeO decreases with increased melting, and increases with increase in pressure, although there is considerable scatter in the data. Incompatible minor elements correlate strongly with degree of melting. Data for K_2O and TiO_2 approximate closely to power-law curves calculated assuming total incompatibility in solids during melting. The data for Na_2O show considerable scatter about a power-law curve fitted to the data (not assuming total incompatibility) with no resolvable pressure effect.

Herzberg (1995) and Herzberg & Zhang (1996) have noted the utility of the Al_2O_3 vs CaO/Al_2O_3 diagram for discerning the pressure of origin of ultramafic melts from garnet peridotite. Figure 6a shows Al_2O_3 vs CaO/Al_2O_3 for melting of KR4003. Contours of constant pressure and degree of melting have been fitted to the data by eye. Al_2O_3 decreases significantly with increase in pressure and is useful as an indicator of pressure of melting, whereas CaO/Al_2O_3 is sensitive to degree of melting or source depletion. An important feature of this diagram is that the CaO/Al_2O_3 ratio at which garnet is exhausted in the residue is essentially constant with pressure at ~0·86, that is, very near the bulk CaO/Al_2O_3 of KR4003 at 0·8. This is used below for deducing the composition of komatiite source regions. Another diagram that is useful for identifying source characteristics of ultramafic melts is Al_2O_3/TiO_2 vs CaO/Al_2O_3, as is shown in Fig. 6b. As in Fig. 6a, melting contours are fitted to the data by eye. Low-degree melts have low Al_2O_3/TiO_2 owing to the incompatible nature of TiO_2 and the effect of garnet in withholding Al_2O_3 from the melt. An increase in melting raises Al_2O_3/TiO_2 and lowers CaO/Al_2O_3,
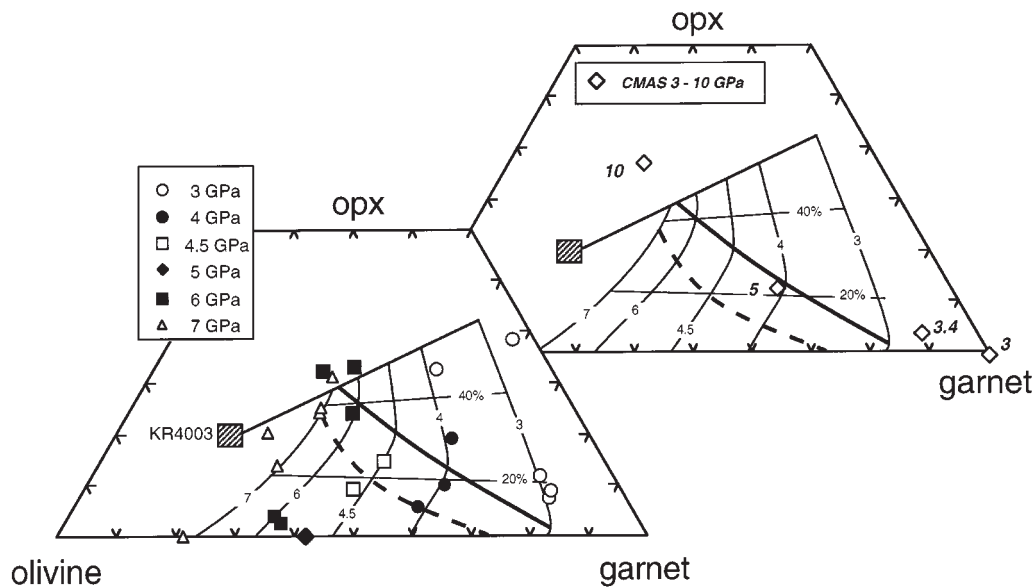
Fig. 4. Molecular normative diagram showing KR4003 melt compositions from 3 to 7 GPa projected from cpx onto opx–olivine–garnet, using the garnet lherzolite norm of Kelemen *et al.* (1992). Isobaric (GPa), percent melting (wt %), and mineral stability contours are fitted to the data by eye. Opx is stable to the opx-rich side of the bold, dashed curve. Garnet is stable to the opx-poor side of the bold, continuous curve. Data for melting of garnet lherzolite in the CMAS system at 3 and 3·4 GPa are from Gudfinnsson & Presnall (1996), and data at 5 and 10 GPa are from Herzberg & Zhang (1997, submitted).

and at the point of garnet exhaustion from the residue melts have $Al_2O_3/TiO_2 > 13$ and $CaO/Al_2O_3 < 0·86$.

ORIGIN OF KOMATIITE

Spinifex-textured high-MgO ultramafic rocks, komatiites, have erupted from early Archean to Cretaceous, and may provide a record of the compositional and thermal evolution of the mantle. On the basis of experimental evidence it is known that komatiitic magmas can be generated by melting of peridotite in the upper mantle or transition zone at pressures in the range of 3–15 GPa (e.g. Takahashi & Scarfe, 1985; Takahashi, 1986, 1990; Wei *et al.*, 1990; Herzberg, 1992, 1995). Currently prevailing models specify that komatiites were generated in upwelling plumes of hot mantle material, perhaps analogous to melting processes operating at modern 'hotspot' locations (e.g. Arndt, 1977; Campbell *et al.*, 1989; Takahashi, 1990; Herzberg, 1992, 1995; Arndt *et al.*, 1997). It has been postulated that komatiite magmas track the history of the cooling of Earth's interior, with early Archean komatiites generated at the highest pressures and temperatures and Cretaceous komatiites along with modern picritic and high-MgO magmas derived at lower pressures and temperatures (e.g. Takahashi, 1990; Arndt & Lesher, 1992; Herzberg, 1992, 1995).

Komatiite data set

Here, constraints on the origin of komatiites are made by comparing phase equilibrium data from KR4003 (i.e. pyrolitic mantle), with a representative data set of komatiite magmas from early Archean to Cretaceous. The data set includes komatiites from Barberton greenstone belt, South Africa (~3·5 Ga), Belingwe greenstone belt, Zimbabwe (~2·7 GPa), Munro, Newton and Tisdale Townships, Canada (~2·7 Ga), Pilbara and Yilgarn, Western Australia (~3·5 and ~2·7 Ga, respectively) and Gorgona Island (~0·12 Ga). All data are from the literature and the sources are listed in the caption to Fig. 7. Nearly all komatiite compositions in the data set are aphyric or spinifex-textured ultramafic lavas. Komatiite taxonomy can be confusing, and here a bi-modal classification is adopted. Alumina undepleted komatiites (AUKs) typically have CaO/Al_2O_3 (wt %) of ~1 or less, have Al_2O_3/TiO_2 (wt %) of ~15–20, and have Gd/Yb_n (normalized to chondritic Gd/Yb) of ~1. Alumina depleted komatiites (ADKs) have $CaO/Al_2O_3 > 1$, have Al_2O_3/TiO_2 of $<10–15$, and are characterized by $Gd/Yb_n > 1$.

Primary komatiite magmas from all locations have undergone crystallization differentiation. Further, Archean komatiites are invariably metamorphosed and alteration has led to mobilization of some elements. It is shown below (see section 'Komatiite Source Composition: Data Reliability') that olivine-control is predominant in
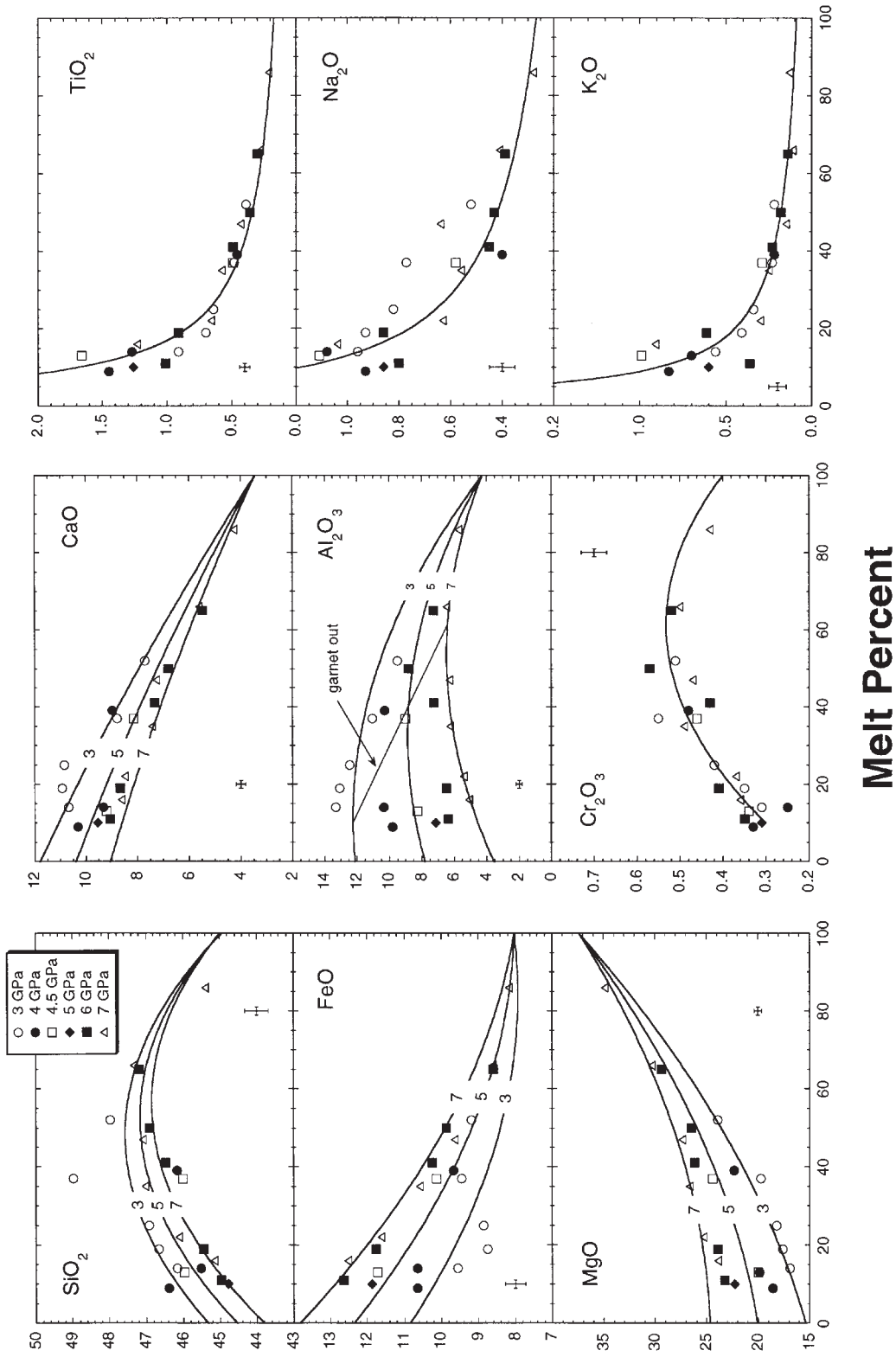
Fig. 5. Variation diagrams showing oxide abundances vs melt percent (wt %). Isobaric melting contours (GPa) for SiO_2, FeO, MgO, CaO and Al_2O_3 are least-squares second-order polynomial best fits to all the data. The polynomial for Cr_2O_3 is not fitted to the data but is schematic. Power-law curves for TiO_2 and K_2O are calculated on the basis of their abundances in the bulk composition and assuming total incompatibility. A power-law curve is fitted directly to the Na_2O data. Error bars show average uncertainties.
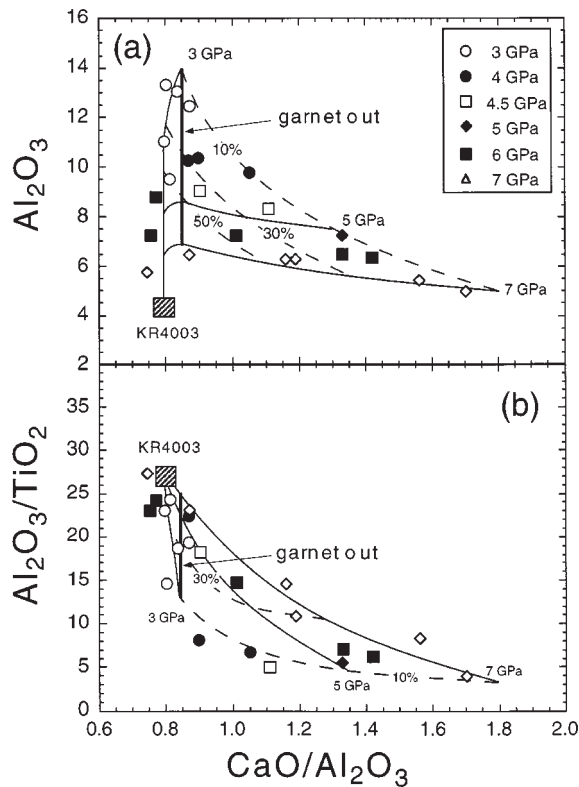
Fig. 6. (a) Al_2O_3 vs CaO/Al_2O_3 and (b) Al_2O_3/TiO_2 vs CaO/Al_2O_3, in wt %, showing melt compositions from KR4003. Isobars (thin continuous lines) and percent melting contours (thin dashed lines) are fitted to the data by eye. Garnet is stable in the residue to the right of the bold, continuous line, and is eliminated from the residue at a constant CaO/Al_2O_3 of ~0·86.

Fig. 7. (a) Al_2O_3 vs CaO/Al_2O_3, showing komatiites relative to the melting contours from Fig. 6a. Data from Gorgona (Cretaceous: Aitken & Echeverria, 1984), Belingwe (late Archean: Nisbet et al., 1987; Bickle et al., 1993), Canada (◆, Munro Township, late Archean: Nesbitt & Sun, 1976; Arndt et al., 1977; Arth et al., 1977; Cattell & Arndt, 1987; Xie et al., 1993), Western Australia (▲, Yilgarn, late Archean: Hallberg & Williams, 1972; Nesbitt & Sun, 1976; Sun & Nesbitt, 1978) and Barberton (■, early Archean: Sun & Nesbitt, 1978; Williams & Furnell, 1979; Smith & Erlank, 1982) are alumina undepleted komatiites (AUKs). Data from Canada (◇, Newton and Tisdale Townships, late Archean: Cattell & Arndt, 1987; Xie et al., 1993), Western Australia (△, Pilbara, early Archean: Nesbitt et al., 1979) and Barberton (□, early Archean: Sun & Nesbitt, 1978; Nesbitt et al., 1979; Smith & Erlank, 1982) are alumina depleted komatiites (ADKs). Two ADKs have CaO/Al_2O_3 >2 and are not shown, one each from Barberton and Pilbara. Filled symbols are from localities where some samples are known to have Gd/Yb_n of ~1, and open symbols are from localities known to have Gd/Yb_n >1. Estimated primary magmas from Gorgona (large open circle) and Belingwe (large shaded circle) are also shown. (b) Al_2O_3/TiO_2 vs CaO/Al_2O_3 for average komatiites from each location relative to KR4003 melting contours. Error bars are one standard deviation from the mean.

data from all locations, and element mobility has not affected significantly the selected data. The ratios CaO/Al_2O_3, Al_2O_3/TiO_2 and Gd/Yb are not fractionated by olivine subtraction or addition, but are sensitive to pressure of melting, degree of melting, and residual source mineralogy (especially residual garnet). These chemical parameters, along with Al_2O_3, are used for deducing the conditions of origin for komatiite.

Melting process

Experimental data for equilibrium melting of KR4003 can be applied quantitatively to komatiite genesis, strictly speaking, only within the context of isobaric batch melting of a fertile source. The melting and segregation processes by which komatiites are generated are not well constrained, and complex polybaric fractional melting scenarios, such as dynamic melting and source depletion, are viable mechanisms. A quantitative assessment of the effect of the melting process using this data set is not possible, but it is possible to predict qualitatively the effect on melt

composition that polybaric near-fractional melting will have relative to batch melting. Kinzler & Grove (1992b) made a quantitative assessment of polybaric near-fractional melting of spinel and plagioclase lherzolite, and generalizations from their results provide a basis for making predictions at higher pressures. For example, in their data set, for a constant degree of batch melting, FeO increases and SiO_2 decreases with increasing pressure. Kinzler & Grove found that accumulated polybaric fractional melts are higher in FeO and lower in SiO_2 than

in the case of batch melting to an equivalent degree at the average pressure in the melting column. Further, incompatible elements such as TiO_2 and Na_2O are enriched in accumulated melts. By extension of these finding to garnet peridotite melting, one can predict that, because high-pressure melts are depleted in garnet components, an accumulated polybaric near-fractional melt will have lower Al_2O_3 and Al_2O_3/TiO_2, and higher CaO/Al_2O_3, than would a batch melt to an equivalent degree at the average pressure of melting. The complementary effects of such dynamic melting on source depletion are discussed below.

Conditions of komatiite genesis

Figure 7a shows komatiite compositions relative to the melting contours from Fig. 6a. Olivine-control lines are vertical on this diagram because olivine fractionation does not change CaO/Al_2O_3, but increases Al_2O_3. Model primary magmas, estimated on the basis of Mg-rich olivines, are shown for Gorgona and Belingwe (large symbols). For batch melting of pyrolite, early Archean komatiites can be generated at 8–10 GPa (10–30% melting), late Archean komatiites, as exemplified by those from Belingwe for example, at ~7 GPa (30 to >50% melting), and Cretaceous komatiites from Gorgona at ~4 GPa (~30% melting). Herzberg (1995) deduced similar pressures of melt generation for komatiites from these localities using this type of diagram for melts from KLB-1. These estimates of pressure and degree of melting lose their specific meaning in dynamic melting processes. However, Al_2O_3 will be sensitive to pressure of melting in either batch or dynamic melting, so the general signature of highest pressure melting in the early Archean to lowest pressure melting in the Cretaceous is robust. Herzberg (1995) suggested that variations in Al_2O_3 and CaO/Al_2O_3 in komatiite melts reflect a secular change in the pressure and temperature of intersection of the peridotite solidus in upwelling plumes of hot mantle material (see also Takahashi, 1990; Arndt & Lesher, 1992), and considered that Hawaii and Iceland are modern representations of this type of plume-related melting. However, it is shown below that there are some geochemical features that cannot be explained within the context of melting of a pyrolitic source.

Komatiite source composition

Garnet has Gd/Yb of ~0·15 (e.g. Hauri & Hart, 1995), and any garnet in the residue of melting produces an increase of Gd/Yb in the melt relative to the source. Although REE abundances are not available for all specimens in the komatiite data set, it is clear that AUKs from Canada, Western Australia, Belingwe and Barberton have Gd/Yb_n of about unity (where Gd/Yb_n means chondrite normalized) (Sun & Nesbitt, 1978; Jahn et al., 1982; Arndt & Jenner, 1986; Cattell & Arndt, 1987; Xie et al., 1993). Thus, garnet is precluded as a residual phase for komatiites from these locations. However, Fig. 7a shows that for pyrolitic mantle (i.e. near-chondritic CaO/Al_2O_3 and Al_2O_3/TiO_2), garnet would be a stable phase in the residues of nearly all AUKs; that is, they have $CaO/Al_2O_3 > 0·86$. This creates a paradox. How can the trace element signature that precludes garnet in the source region of AUKs be reconciled with their high CaO/Al_2O_3 (i.e. relative to the garnet-out curve)? Conversely, ADKs from Barberton, Canada, and Western Australia have $Gd/Yb_n > 1$ indicating garnet in the residue (Jahn et al., 1982; Cattell & Arndt, 1987; Gruau et al., 1987; Xie et al., 1993), and this is consistent with the high CaO/Al_2O_3 of these lavas.

Figure 7b shows komatiite compositions on a plot of Al_2O_3/TiO_2 vs CaO/Al_2O_3 relative to melting contours for KR4003. For clarity, average komatiite compositions with standard deviations are shown for each location. What we are searching for are conditions that can yield the observed characteristics of high CaO/Al_2O_3 and Al_2O_3/TiO_2 in AUKs, without leaving a garnet-bearing residue. There are several possibilities to consider, including (1) komatiite data reliability, (2) the effect of H_2O on melt composition and garnet stability, (3) dynamic melting and source depletion, and (4) non-pyrolitic source compositions.

Data reliability

Could element mobility during fluid alteration have increased CaO/Al_2O_3 and Al_2O_3/TiO_2 in AUKs away from primary pyrolitic values? Beswick (1982) argued that Si, Al, Fe, Mg, Ca and Ti were essentially immobile during alteration of many Archean komatiites. Lecuyer et al. (1994) found evidence for Ca mobility in highly olivine-phyric rocks from Barberton but concluded that the primary character of Ca/Al and Al/Ti of spinifex-textured samples is preserved. Bickle et al. (1993) and Lahaye & Arndt (1996) have argued for some Ca mobility in AUKs from Belingwe and Alexo, Canada, respectively.

To assess the effects of crystal differentiation and possible element mobility on komatiites, data from each location were plotted on Pearce element ratio diagrams (e.g. Beswick, 1982; Russell et al., 1990). Data were plotted on diagrams of molar (FeO + MgO)/A vs SiO_2/A, where A is the conserved element in a system undergoing differentiation; in this case, CaO, Al_2O_3 or TiO_2. The following deductions can be made from this type of diagram: (1) ferro-magnesian silicate minerals with different stoichiometries generate linear trends with distinct slopes (e.g. olivine-control generates a trend with a slope of 0·5); (2) systematic but variable addition or

Table 10: Pearce element ratio analysis of komatiites

Location	n*	Element†		
		Ca	Al	Ti
Gorgona (AUK)	11	0·50 (0·99)‡	0·50 (0·99)	0·56 (0·97)
Belingwe (AUK)	17	0·48 (0·98)	0·50 (0·99)	0·51 (0·98)
W. Australia (AUK)	13	0·52 (0·99)	0·48 (0·98)	0·54 (0·97)
W. Australia (ADK)	3	0·46 (0·90)	0·42 (0·77)	1·17 (0·43)
Canada (AUK)	15	0·62 (0·98)	0·65 (0·97)	0·66 (0·92)
Canada (ADK)§	3	0·63 (0·99)	0·35 (0·97)	0·56 (1·00)
Barberton (AUK)	3	0·52 (0·99)	0·51 (0·98)	0·56 (0·96)
Barberton (ADK)	16	0·59 (0·99)	0·46 (0·91)	0·47 (0·93)

*Number of komatiite data points.
†Element being tested for effects of differentiation during crystal fractionation or alteration, using plots of molar SiO_2/A vs $(FeO+MgO)/A$, where A is CaO, Al_2O_3 or TiO_2.
‡Given are the slopes of best-fit linear trends and, in parentheses, the regression coefficients, R^2.
§Data from Newton Township.

subtraction of element A in a stoichiometric alteration process can either increase or decrease the slope of mineral-control trends, but previous linear correlations owing to crystal fractionation are preserved; (3) non-stoichiometric, random addition and subtraction of element A will cause dispersion about mineral-control trends.

The results of Pearce element ratio analysis are given in Table 10. Highly correlated trends with slopes near 0·5 are seen for AUKs from Gorgona, Belingwe and Western Australia. This is consistent with olivine-control at these locations, and no significant element fractionations as a consequence of alteration are indicated. The trends for AUKs from Canada are significantly correlated, but the slopes for all elements, although very similar to each other (0·62–0·66), are significantly higher than 0·5. This indicates the operation of some process other than olivine fractionation. Whatever the process, alteration or crystal differentiation, the coincidence of slopes for all elements suggests a process in which these elements are conserved, so that near-primary ratios would be preserved. There are only three AUKs from Barberton in the data set, and these have the highest CaO/Al_2O_3 of any reported AUKs in the world. Conclusions drawn from these samples are tentative and must be verified by more AUKs from the early Archean. However, CaO, Al_2O_3 and TiO_2 have a relatively large range in these three samples, and they define highly correlated trends consistent with olivine-control, with little indication of element mobility.

Olivine-control is also indicated in ADKs from Barberton, but some other process is also evident. There is some evidence of olivine-control in ADKs from Western Australia and Canada (Newton Township), but too few data make interpretations ambiguous. Inasmuch as the CaO/Al_2O_3 values of these ADKs are not enigmatic with respect to garnet stability, these features are not considered further, but primary ratios are considered to lie within the error bars shown in Fig. 7b.

Overall, olivine-control is strongly indicated in this data set, and there is no suggestion of pervasive mobility of CaO, Al_2O_3 or TiO_2. Moreover, the average compositions from inter-craton late Archean locations are virtually indistinguishable from each other, well within uncertainty. If element mobility were a pervasive problem, this would be an unlikely coincidence. Thus, CaO/Al_2O_3 and Al_2O_3/TiO_2 of komatiites in this data set are considered to be near-primary.

Hydrous melting

Recently, evidence has been presented for a possible important role for water in komatiite generation (Grove *et al.*, 1994; Stone *et al.*, 1997). There are limited experimental data for the effect of H_2O on peridotite phase relations and melt chemistry at high pressures. Kawamoto & Holloway (1997) presented data for H_2O-saturated melting of KLB-1. Their results at 5 and 7·5 GPa show that H_2O saturation increases significantly the CaO/Al_2O_3 of near-solidus melts relative to dry melting. At 5 GPa, they found that garnet is stable up to ~40% melting, very similar to KR4003, and that when garnet is exhausted in the residue, CaO/Al_2O_3 in the melt is ~1·0 and Al_2O_3/TiO_2 is ~19, just marginally different from the bulk composition, KLB-1 (CaO/Al_2O_3 = 0·96

and $Al_2O_3/TiO_2 = 23$). Their results indicate that garnet stability is similar during anhydrous and hydrous melting and, regardless of whether melting is wet or dry, when garnet is eliminated from the residue both CaO/Al_2O_3 and Al_2O_3/TiO_2 will be close to the source composition. Water-saturated melting of pyrolitic mantle cannot account for unusually high CaO/Al_2O_3 melts from a garnet-free source, and it is doubtful that lower water contents will significantly alter garnet stability if large amounts do not.

Dynamic melting

On the basis of extreme depletions in magmaphile trace elements, Arndt *et al.* (1997) have proposed that komatiitic rocks from Gorgona are the products of melting of peridotite previously depleted in melt. Extreme depletions have been observed in Archean komatiites as well, and depleted source models have also been proposed for these (e.g. Sun & Nesbitt, 1978). Arndt *et al.* envisioned a dynamic melting process in which low-degree melts are continuously removed from the core of a plume as it rises, and from which only lower-pressure melts are buoyant enough to segregate to erupt as komatiites. As discussed above, dynamic melting should produce accumulated melts with lower Al_2O_3 and Al_2O_3/TiO_2, and higher CaO/Al_2O_3 than produced by 'equivalent' batch melting. Could the paradoxically high CaO/Al_2O_3 (relative to the garnet-out curve for pyrolite) of the AUKs be an artifact of dynamic melting and source depletion? Extraction of melts depleted in garnet components (low Al_2O_3 and Al_2O_3/TiO_2, and high CaO/Al_2O_3) in the high-pressure portion of a dynamic melting zone will result in relatively higher Al_2O_3 and lower CaO/Al_2O_3 in the lower-pressure residues. This should stabilize garnet in the residue to overall higher degrees of melt depletion relative to batch melting, and the CaO/Al_2O_3 at which garnet is exhausted may even decrease. Low-degree melts from residual peridotite previously depleted at higher pressures should have relatively lower CaO/Al_2O_3 and higher Al_2O_3/TiO_2, as a consequence of melting a depleted source with enhanced garnet component. This qualitative argument indicates that dynamic melting will only reinforce the paradox. This does not imply that dynamic melting was not important in komatiite generation, only that it apparently cannot account for combined $CaO/Al_2O_3 > 1{\cdot}0$ with Gd/Yb_n of about unity.

Non-pyrolitic source compositions

Shown in Fig. 8 are estimated source compositions that can account for the paradox in question. The estimates were made assuming that the general topology of the melting trend from Fig. 6b remains essentially constant with change in composition, a likely condition for these ratios. A further criterion is that AUKs must plot to the left of the garnet-out line and ADKs to the right. The position of the garnet-out curve may shift proportionally with bulk composition, but higher CaO/Al_2O_3 will result in a source with a higher pyroxene/garnet ratio in the source rock, and the garnet-out curve may shift to higher CaO/Al_2O_3 (lower degrees of melting). If CaO/Al_2O_3 in the source region were about unity, then garnet would not be expected to be a residual phase during melting to produce late Archean AUKs, but would remain in the residue of late Archean ADKs from Canada because they would be generated by relatively lower degrees of melting. A CaO/Al_2O_3 of $\sim 1{\cdot}4$ is indicated for early Archean komatiites. If the garnet-out curve moves to higher CaO/Al_2O_3, as shown schematically, then garnet would not be expected to remain in the source of AUKs, but would in the ADKs generated by lower degrees of melting. It is emphasized that phase relations of peridotite compositions with higher CaO/Al_2O_3 are necessary to confirm these predictions in detail.

Within the framework of a variable source model, secular variation in the mantle source of komatiites is indicated. Further, within a given time period, the compositional differences between ADKs and AUKs (i.e. CaO/Al_2O_3, Al_2O_3/TiO_2 and Gd/Yb) do not require variation in pressure of melting, but can be accounted for by variable degrees of melting (or, alternatively, variable source depletion). For example, ADKs can be generated by relatively lower degrees of melting leaving garnet in the residue, and AUKs can be generated by higher degrees of melting leaving a garnet-free residue.

Speculations

CaO/Al_2O_3 and Al_2O_3/TiO_2 are near-chondritic in pyrolitic mantle, implying that early Archean komatiite source rocks may have had very non-chondritic refractory element ratios. What process could have resulted in such non-chondritic komatiite source regions? Variation in CaO/Al_2O_3 and Al_2O_3/TiO_2 could indicate large-scale spatial heterogeneities in the mantle, as has been suggested on the basis of both inter- and intra-regional variations in komatiite trace element chemistry (e.g. Jahn *et al.*, 1982; Xie *et al.*, 1993). In this case, the apparent secular variations in these ratios would be an artifact. Alternatively, secular variations in the composition of komatiite source rocks could reflect chemical evolution in the mantle (Jahn *et al.*, 1982), or chemical evolution in whatever material was incorporated in ascending plumes.

Early Archean komatiites are among the oldest rocks on Earth, and the processes by which komatiite source regions formed are necessarily even older. There are no direct samples from the mantle for the first billion years or so of the Earth's history, so all models for Archean source regions are speculative and difficult to test. Two
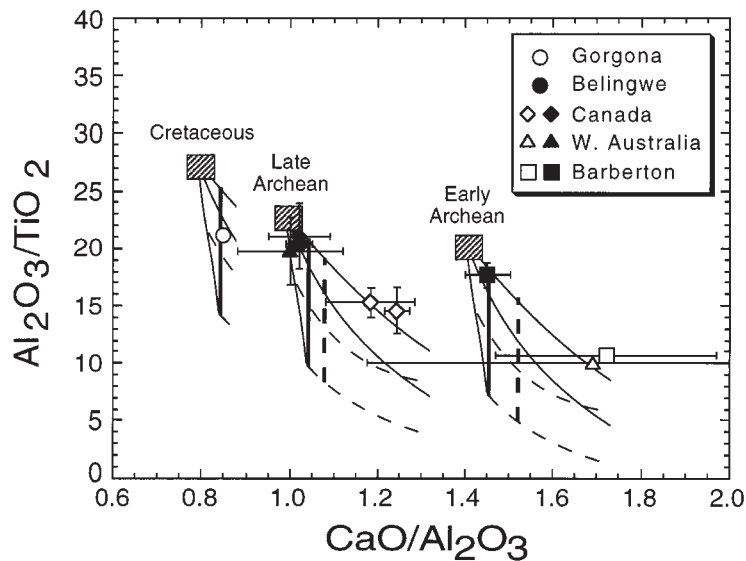
Fig. 8. Al_2O_3/TiO_2 vs CaO/Al_2O_3 (wt %) showing estimated source compositions for early Archean, late Archean, and Cretaceous komatiites, respectively. A portion of the melting trend from Fig. 6b has been superimposed for each estimated source. Bold dashed lines schematically show shifts in the garnet out curve to lower degrees of melting for sources with CaO/Al_2O_3 greater than pyrolite.

general possibilities are considered here, involving (1) primordial mantle heterogeneity, and (2) plume heterogeneity.

Primordial mantle heterogeneity

Most of Earth's mass probably accreted during the first 200 my or so as large objects with diameters from tens to hundreds of kilometers (e.g. Wetherill, 1985). It is conceivable that these objects imparted large-scale spatial heterogeneity to the mantle. Although there are few hard constraints on the exact nature of accreting material, there is compelling geochemical and isotopic evidence that many refractory trace element ratios were near-chondritic in the Archean mantle (e.g. Lu/Hf, Sm/Nd, Re/Os; McDonough & Sun, 1995). Also, no groups of primitive chondritic meteorites have $CaO/Al_2O_3 > 0.88$, although some differentiated achondrites have $CaO/Al_2O_3 > 1.6$. At present, there is no corroborating evidence for large-scale spatial heterogeneity in the mantle resulting from accretionary processes.

A more probable mechanism for the formation of pre-Archean mantle heterogeneities is that crystallization differentiation of mantle liquidus phases during a Hadean magma ocean stage fractionated refractory element ratios away from initially chondritic values. In this hypothesis, komatiite source regions could have had their origins as residual melts. The effects of fractional crystallization of upper-mantle, transition zone and lower-mantle liquidus phases on refractory element ratios have been calculated by many workers (e.g. Ito & Takahashi, 1987; Agee & Walker, 1988; Herzberg et al., 1988; Kato et al., 1988;

Ohtani et al., 1989; Agee, 1993; McFarlane et al., 1994; Presnall et al., 1997). Extensive fractionation of olivine in the upper mantle does not fractionate Ca, Al, and Ti in residual melts, whereas majorite fractionation would lead to residual melts with high CaO/Al_2O_3, but with $Gd/Yb_n \gg 1$, which is not indicated in the AUKs. Thus, these mechanisms do not produce satisfactory sources for AUKs.

The effects of fractional crystallization of Mg-perovskite and magnesiowustite in the lower mantle on initially chondritic refractory element ratios can be calculated using the mineral–melt partition coefficients measured by McFarlane et al. (1994), and assuming an 85:15 crystallization mixture of Mg-perovskite and magnesiowustite (Presnall et al., 1997); 50% crystallization would increase CaO/Al_2O_3 from 0.8 to 1.32 and Al_2O_3/TiO_2 from 22.3 to 22.7. These fractionated values are strikingly similar to the estimate for the early Archean source based on Fig. 8. If this model is correct, then near-chondritic refractory element ratios in modern pyrolitic mantle do not indicate a continuity of these ratios from primeval values, but instead might record processes of convective mixing and re-homogenization of originally heterogeneous but bulk chondritic mantle (e.g. Ohtani et al., 1989). However, at present this model causes more problems than it solves. Measured partition coefficients between Mg-perovskite and ultramafic melt show that, besides CaO/Al_2O_3 and Al_2O_3/TiO_2, other refractory element ratios such as Lu/Hf, Sc/Sm, and Ti/Sm would become significantly fractionated from chondritic values, even at rather modest amounts (e.g. <20%) of crystallization of Mg-perovskite (Kato et al., 1988; McFarlane

et al., 1994). However, near-chondritic refractory trace element abundance ratios and primitive isotopic compositions in some komatiites are antithetical to extensive fractional crystallization of transition zone or lower-mantle liquidus phases in the Hadean (e.g. Jahn *et al.*, 1982; Gruau *et al.*, 1987). Precise partitioning data over a wide range of lower-mantle pressures and temperatures coupled with complete data for trace element abundances in komatiites are required to test this model more strictly.

Plume heterogeneity

Komatiites could be the products of plume-related melting, analogous to processes at modern 'hot-spots'. By extension of modern plate tectonics theory, the material forming the plumes might have been composed substantially of material processed at shallow levels and recycled into the mantle through Archean or pre-Archean subduction zones. To account for Gd/Yb_n of ~1 coupled with the high CaO/Al_2O_3 in Archean komatiites by this hypothesis, the recycled material must have had high CaO/Al_2O_3 without a history of garnet fractionation. Low-degree partial melts of spinel lherzolite can have very low CaO/Al_2O_3 (<0·5, Kinzler & Grove, 1992*b*), and residues of fractional melting will have increased CaO/Al_2O_3. For example, modern examples of depleted abyssal peridotites, which have undergone near-fractional melt extraction at low pressures (Johnson *et al.*, 1990) and make up much of the oceanic lithosphere, have reconstructed CaO/Al_2O_3 ranging from ~0·8 to 1·1 (e.g. Dick, 1989). However, few constraints on the composition of material subducted in the Archean or pre-Archean can be made, so this model is implicitly *ad hoc*.

Hot upwelling plumes incorporate material as they travel through the mantle, and also when a plume-head develops as a consequence of impingement on a thermal boundary layer, such as the lithosphere (e.g. Campbell *et al.*, 1989). The entrained material, and that encompassed by and adjacent to the plume head, is subject to heating and melting; a type of thermal erosion. The material consumed in this way may have a significantly different composition from that in the core of the upwelling plume. As with the previous hypothesis, postulating compositions is *ad hoc*. For example, pyroxene-rich cumulates crystallized from a Hadean magma ocean at low pressures would have had much higher than chondritic CaO/Al_2O_3, and Gd/Yb_n of ~1. Or, if a proto-crust with low CaO/Al_2O_3 were formed in the Hadean, the residue would have had high CaO/Al_2O_3. The existence of such cumulates or residues is mere speculation. However, an interesting feature of this hypothesis is that if the temperature of upwelling plumes decreases with time in a cooling Earth, then the amount of material digested by the plume would decrease accordingly, leading to secular variation in the overall plume composition and

recovery of near-chondritic values as the amount of entrained material drops to zero (at least in the central portion of the plume producing komatiites), thus providing an explanation why the youngest komatiites are near-chondritic.

At present, there is no compelling model to account for komatiite source regions with CaO/Al_2O_3 significantly higher than chondritic. However, given that the komatiite data are reliable, an explanation of this feature could reveal much about the nature and evolution of mantle source regions.

ORIGIN OF DEPLETED PERIDOTITE

The extraction of mafic and ultramafic melts from fertile peridotite leaves behind a depleted residue, the composition of which is determined by the initial peridotite composition and the melt composition at the conditions of segregation. Peridotite xenoliths, abyssal peridotites, alpine peridotites and ophiolite peridotites are pieces of the mantle that were transported to the Earth's surface in a variety of ways, and they provide a glimpse into the composition and structure of the uppermost part of the mantle. Many of these diverse samples are depleted relative to models of fertile mantle material such as pyrolite, having mineralogical, major and trace element characteristics consistent with an origin as residues from melting (e.g. Dick & Fisher, 1984; Bonatti & Michael, 1989; Boyd, 1989; Dick, 1989; Johnson *et al.*, 1990). In general, samples of depleted upper-mantle lithosphere can be differentiated into two broad compositional groups: oceanic and cratonic (see Boyd, 1989).

As defined by Boyd (1989), the fundamental distinction between these two groups is that peridotites from oceanic lithosphere are olivine rich with *mg*-numbers typically in the range of 90·5–91·5, whereas peridotites from cratonic lithosphere are enstatite rich and have *mg*-numbers in the range of 91·5–93·5. Abyssal peridotites, most alpine and ophiolite peridotites, many oceanic peridotite xenoliths, and sub-continental xenoliths from cratonic margins fall along an 'oceanic' trend, and this trend is consistent with melt extraction from fertile pyrolitic mantle at relatively low pressures (Boyd, 1989). High-temperature (>1100°C) deformed peridotite xenoliths, and coarse, low-temperature peridotites (<1100°C) from the Kaapvaal craton in southern Africa and from Udachnaya in the Siberian craton, form the cratonic peridotite suite (Cox *et al.*, 1973; Boyd & Nixon, 1978; Carswell *et al.*, 1979; Danchin, 1979; Boyd, 1984; Boyd & Mertzman, 1987; Boyd *et al.*, 1997). High-temperature peridotites plot close to the oceanic trend (see below), and only low-temperature peridotites are clearly distinct from oceanic peridotites as defined above. In the discussion that follows, however, both high- and low-temperature peridotites

from southern Africa and Siberia are referred to as cratonic peridotite.

Whereas oceanic peridotites have been interpreted in terms of melt extraction at low pressures from pyrolitic source material, the origin of cratonic peridotites remains enigmatic; the principal challenge is to find a process that can produce a coupling between high *mg*-number and high enstatite content. Many processes have been proposed to explain the origin of cratonic peridotites, including: (1) residues of komatiite melt extraction (Boyd & Mertzman, 1987; Boyd, 1989; Walker *et al.*, 1989; Canil, 1991, 1992; Herzberg, 1993); (2) mechanical sorting, including cumulates from ultramafic melts (Boyd & Mertzman, 1987; Herzberg, 1993) and metamorphic differentiation (e.g. Boyd, 1989; Boyd *et al.*, 1997); (3) exsolution (Dawson *et al.*, 1980; Cox *et al.*, 1987; Canil, 1991); (4) mantle–melt reactions (Kelemen *et al.*, 1992; Rudnick *et al.*, 1994; Kelemen & Hart, 1996); (5) majorite fractionation (Herzberg *et al.*, 1988); (6) mantle overturn (Griffin *et al.*, 1997); (7) fluid metasomatism (Kesson & Ringwood, 1989). None of these processes are mutually exclusive. Here, the residue hypothesis for the origin of oceanic and cratonic peridotites is tested by comparison with residues produced by melting of pyrolitic mantle.

Figure 9a is a plot of MgO/SiO_2 vs SiO_2 showing African and Siberian low-temperature cratonic peridotites. Also shown are the residue trends for melting of KR4003 (pyrolitic mantle) and a mixing trend between olivine and opx. Clearly, the data do not follow the residue trend, but are distributed about the mixing trend. Thus, most of the compositional variability can be attributed to variations in olivine and opx content unrelated to melting. Boyd *et al.* (1997) found a negative correlation between FeO and SiO_2 in the Udachnaya data that is consistent with mixing between olivine and opx. Data for KR4003 show that melting of garnet lherzolite produces a positive trend between these elements in residues, and this is also true for melting throughout much of the spinel lherzolite field. An olivine–opx mixing trend can be consistent with a melt–mantle reaction process wherein olivine is consumed and opx is crystallized (e.g. Kelemen *et al.*, 1992), or it could imply a mechanical sorting process. Boyd *et al.* found no significant correlation between Ni in olivine and modal opx in the Udachnaya data set, as would be expected from mantle–melt interaction (Kelemen & Hart, 1996), and proposed that processes such as cumulate mixing or metamorphic sorting (i.e. unmixing) could account for the FeO–SiO_2 trend. Boyd *et al.* suggested a residual model for cratonic lithosphere, with subsequent metamorphic sorting, because of the depleted major element characteristics of cratonic peridotites, and because there is a distinction between lherzolites and harzburgites from southern Africa that is consistent with melt extraction. That is, at a given SiO_2 content, lherzolites have a higher FeO content than harzburgites, and

this is consistent with the positive relationship between these elements expected in high-pressure melting residues. If low-temperature peridotites are melting residues, and if the compositional variation observed in Fig. 9a is a result primarily of metamorphic sorting, then given sufficient sampling coverage, the average compositions of low-temperature peridotites from Siberia and southern Africa may represent adequately the bulk residues of large-scale melt extraction events. This assumption is implicit in Figs 10 and 11. In contrast to low-temperature peridotites, Fig. 9b shows that high-temperature peridotites, as a group, plot close to the residual melting trend for pyrolitic mantle.

Figure 10a is a plot of whole-rock *mg*-number vs modal olivine (wt %) showing both oceanic and average cratonic peridotites relative to pyrolite residue trends for melting from 2 to 7 GPa. A garnet lherzolite normative calculation (Kelemen *et al.*, 1992) was applied to the whole-rock compositions of all data points and to experimental residues, to compare equivalent mineral components among all compositions. This is necessary because the experimental residues and the diverse group of mantle samples have equilibrated over a wide range of pressures and temperatures. Oceanic peridotites plot close to a 2 GPa residue trend (based on the experimental data for melting of KLB-1; Hirose & Kushiro, 1993) and this is consistent with melt extraction from pyrolitic mantle at low average pressures beneath mid-ocean ridges (e.g. Klein & Langmuir, 1987). High-temperature cratonic peridotites plot close to the oceanic trend, indicating melt extraction at 2–3 GPa. The high *mg*-numbers of average low-temperature cratonic peridotites indicate high-pressure melt extraction. The average Udachnaya composition could be a residue of melt extraction from a pyrolitic source at ~6 GPa and 40% melting, and the Kaapvaal composition could be a residue of higher-pressure melting, perhaps 9 GPa and 40% melt extraction.

Figure 10b is a plot of whole-rock *mg*-number vs modal opx content. Oceanic peridotites are consistent with melt extraction at low pressures. The elevated opx component in high-temperature cratonic peridotites, relative to oceanic peridotites at similar *mg*-numbers, indicates melt extraction at somewhat higher pressures. Figure 10 indicates that high-temperature peridotites are residues of melt extraction at 2–3 GPa. In the high-pressure portion of the spinel lherzolite field (1·5–2·5 GPa), opx crystallizes during melting of lherzolite by a peritectic reaction of the form cpx + spinel = melt + olivine + opx (Kinzler & Grove, 1992*a*; Bertka & Holloway, 1993; Walter *et al.*, 1995*a*). This reaction can explain the higher opx component in high-temperature peridotites relative to the oceanic trend. Thus, high-temperature peridotites record a history of melt extraction at relatively low
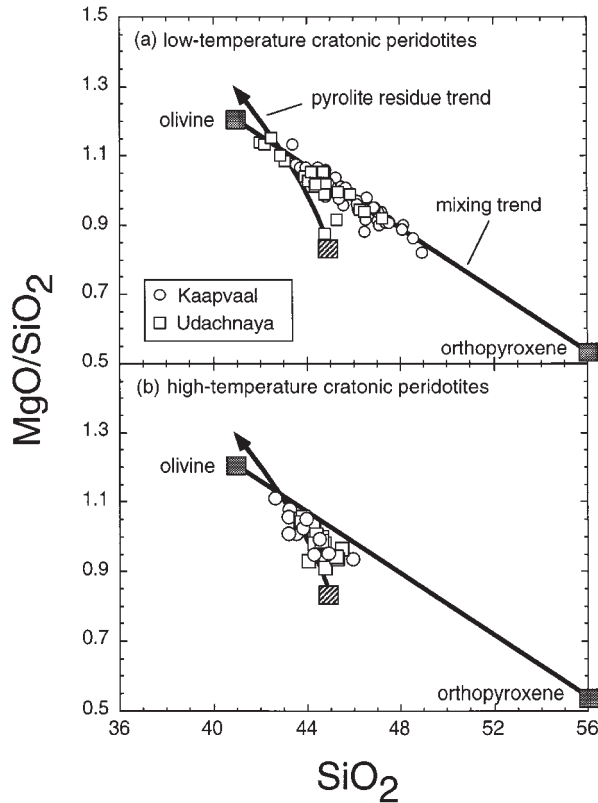
Fig. 9. (a) MgO/SiO_2 vs SiO_2 (wt %) showing low-temperature peridotites from Kaapvaal, southern Africa, and Udachnaya, Siberia, relative to the residue trend for pyrolitic mantle (KR4003), and to a mixing trend between olivine and opx (olivine and opx compositions are approximations from compositions observed in xenoliths). (b) High-temperature peridotites from Kaapvaal and Udachnaya shown relative to the pyrolite residue and ol–opx mixing trends.

pressures, and their protoliths may have originated in the oceanic lithosphere (Boyd & Mertzman, 1987).

In Fig. 10b, average Udachnaya low-temperature peridotite plots very close to the field of pyrolite residues but is slightly enriched in opx. It can be a residue of ~40% melting, as indicated also in Fig. 10a, although the scatter of the experimental data (not shown) precludes a clear distinction of a pressure effect in the residue trend. At 6 GPa and 40% melting, the melt composition is komatiite and, therefore, it is possible to explain the composition of average Siberian cratonic lithosphere as a residue of komatiite extraction from pyrolitic mantle, or a composition slightly enriched in SiO_2 relative to pyrolite. This, however, is clearly not the case for average Kaapvaal low-temperature peridotite as the opx component is much higher than can occur in residues of pyrolite. If Kaapvaal peridotite is a residue of anhydrous melting, then the initial peridotite composition must have had a higher opx component than pyrolitic mantle (Kelemen *et al.*, 1992; Herzberg, 1993). Herzberg (1993) suggested that the initial peridotite would have needed an SiO_2 content of 48 wt %. A similar model is shown schematically in Fig. 11. It should be noted that high-temperature

peridotites and average Siberian low-temperature peridotite fall close to the pyrolite trend, whereas Kaapvaal low-temperature peridotite plots at a significantly higher SiO_2 content. Predicting the exact residue trend for a bulk composition with a higher SiO_2 content is not straightforward because of uncertainty about the SiO_2 content of the melt. However, a Kaapvaal source composition is estimated by assuming a 50:50 mixture of average Barberton komatiite and average Kaapvaal low-temperature peridotite. This source has an SiO_2 content of 46·8 wt % and MgO/SiO_2 of 0·79.

Discussion

The Siberian lithosphere, as represented by the average composition of low-temperature peridotites from Udachnaya, has a composition that can be related to extraction of komatiite magma. Given the similarities in composition (high *mg*-numbers and Si content, Ca and Al depletion), mineralogy, textures and age between the Siberian and southern African lithosphere, a similar genetic history is indicated by analogy (Boyd *et al.*,
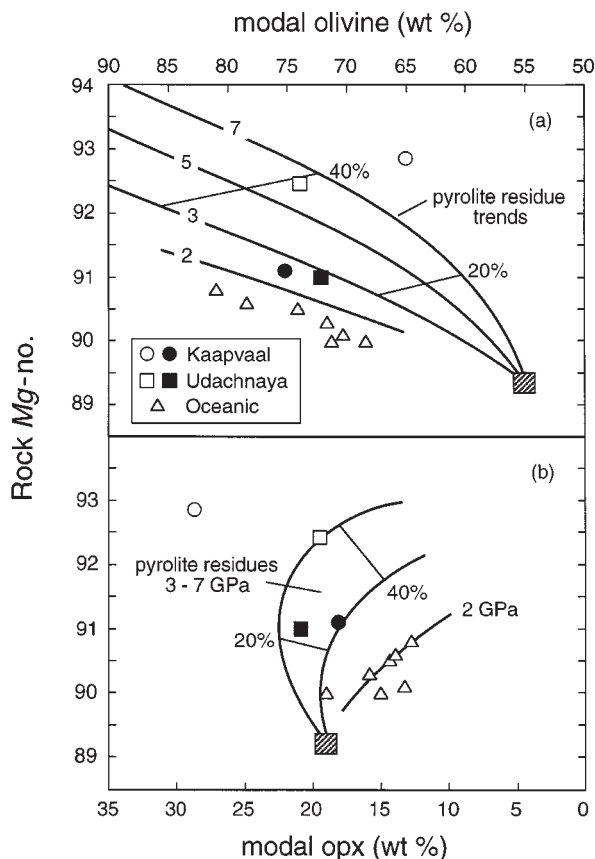
Fig. 10. (a) Whole-rock *mg*-number vs modal olivine (wt %) showing residue trends for melting of pyrolitic mantle (3–7 GPa, KR4003, this study; 2 GPa, KLB-1, Hirose & Kushiro, 1993). Residue contours are labeled according to pressure (GPa) and percent melting. Also shown are 'oceanic' peridotites (average abyssal peridotite, Dick & Fisher, 1984; SW Indian abyssal peridotites, Dick, 1989; average continental and oceanic spinel lherzolites, Maaloe & Aoki, 1977), and average low-temperature (open symbols) and high-temperature peridotites (filled symbols) from Kaapvaal and Udachnaya. Whole-rock *mg*-numbers calculated as $(Mg/Mg + Fe) \times 100$ where $Fe^{2+}/Fe^{3+} = 1$, and using calculated FeO content for peridotites from Kaapvaal and Udachnaya (see Boyd & Mertzman, 1987; Boyd *et al.*, 1997). Modal olivine is calculated from the garnet lherzolite norm of Kelemen *et al.* (1992). (b) Whole-rock *mg*-number vs modal opx [wt %, as calculated from the garnet lherzolite norm of Kelemen *et al.* (1992)] showing oceanic and cratonic peridotites relative to pyrolite residue trends.

1997). The age of both the Siberian and south African lithosphere is estimated at >3·2 Ga on the basis of Re depletion ages from peridotites (Pearson *et al.*, 1995*a*, 1995*b*). The similarity between ages of southern African cratonic lithosphere and komatiites at Barberton suggests a possible genetic relationship between komatiite extraction and lithosphere formation. It is interesting that southern African low-temperature peridotites indicate a unique, non-pyrolitic mantle, at least in SiO_2, and Barberton komatiites also indicate a non-pyrolitic source (at least in CaO/Al_2O_3 and Al_2O_3/TiO_2), whereas the

Siberian lithosphere could have had a near-pyrolitic protolith, at least in SiO_2. This gives some support for models of large-scale spatial heterogeneities in the early Archean mantle (see Herzberg, 1993). Unfortunately, secondary alteration of xenoliths from southern Africa and Siberia has perturbed primary Ca and Ti contents (Boyd & Mertzman, 1987; Boyd *et al.*, 1997), so it is not possible to make a meaningful investigation into CaO/Al_2O_3 and Al_2O_3/TiO_2 relationships in these rocks.

High-temperature peridotites from both Siberia and southern Africa have deeper equilibration depths (~175–200 km) than low-temperature peridotites, and they may represent depleted asthenospheric mantle from below the lithosphere–asthenosphere boundary (e.g. Boyd & Gurney, 1986; Boyd *et al.*, 1997). Figure 10 shows that high-temperature peridotite protoliths could have undergone melt extraction at low pressures (2–3 GPa), perhaps in an oceanic environment. This requires transport and emplacement of oceanic lithosphere beneath cratonic lithosphere, a model that is consistent with a subduction origin for eclogite xenoliths in Kaapvaal kimberlites (Jagoutz *et al.*, 1984).

CONCLUSIONS

(1) Orthopyroxene is not stable at the solidus of pyrolite above ~3·3 GPa, but crystallizes above the solidus by a peritectic melting reaction up to ~10 GPa.

(2) Garnet becomes progressively stable to higher degrees of melting with increase in pressure, replacing opx near the liquidus at ~6·6 GPa. When garnet is exhausted from the residue during melting, the CaO/Al_2O_3 ratio of the residue is essentially constant at ~0·86 (close to the bulk value of 0·8), and is independent of pressure.

(3) The Al_2O_3 contents of komatiites record secular variation in average pressure of melting, as deduced previously by Herzberg (1995). However, data also indicate that Archean komatiite source regions had higher CaO/Al_2O_3 and lower Al_2O_3/TiO_2 than pyrolite, and that early and late Archean source regions were unique from each other, having CaO/Al_2O_3 of about 1·4 and 1·0, respectively. The source of Cretaceous komatiites was probably pyrolitic in these ratios (0·8). These source variations may indicate secular chemical evolution of komatiite source regions or large-scale mantle heterogeneity.

(4) Chemical differences (e.g. Ca/Al, Al/Ti, Gd/Yb) between AUKs and ADKs from a given time period can be explained by melting at similar pressures. AUKs can be generated by high degrees of melting of a fertile source or low degrees of melting of a depleted source, and leaving a garnet-free residue. ADKs can be generated by lower degrees of melting than AUKs, or similar
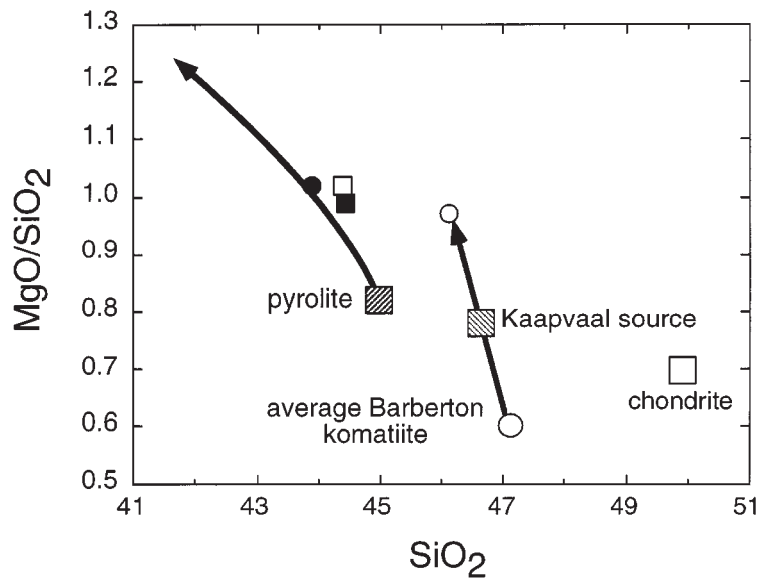
Fig. 11. MgO/SiO$_2$ vs SiO$_2$ (wt %) showing high- and low-temperature cratonic peridotites (symbols as in Fig. 10) relative to the residue trend for melting of pyrolite. Also shown is a hypothetical source composition for Kaapvaal lithosphere constructed by adding 50% average Barberton komatiite to 50% average low-temperature South African peridotite. Chondritic mantle from McDonough & Sun (1995).

degrees of melting of a less depleted source, leaving a garnet-bearing residue.

(5) Depleted oceanic peridotites and high-temperature peridotites from cratons can be residues of melt extraction from pyrolitic mantle at low pressure (<3 GPa). Protoliths of high-temperature cratonic peridotites may have had their origin in the oceanic lithosphere.

(6) Average low-temperature cratonic peridotite from Udachnaya, Siberia, can be a residue of komatiite melt extraction from pyrolitic mantle at ~6 GPa and 40% melting. Average low-temperature peridotite from southern Africa cannot be a melting residue of pyrolitic mantle, but can be a residue of komatiite melt extraction from a source enriched in SiO$_2$ relative to pyrolitic mantle.

REFERENCES

Agee, C. B., (1993). Petrology of the mantle transition zone. *Annual Review of Earth and Planetary Sciences* **21,** 19–41.

Agee, C. B. & Walker, D., (1988). Mass balance and phase density constraints on early differentiation of chondritic mantle. *Earth and Planetary Science Letters* **90,** 144–156.

Agee, C. B., Li, J., Shannon, M. C. & Circone, S., (1995). Pressure–temperature phase diagram for the Allende meteorite. *Journal of Geophysical Research* **100,** 17725–17740.

Aitken, B. G. & Echeverria, L. M., (1984). Petrology and geochemistry of komatiites and tholeiites from Gorgona Island, Colombia. *Contributions to Mineralogy and Petrology* **86,** 94–105.

Arndt, N. T., (1977). Ultrabasic magmas and high-degree melting of the mantle. *Contributions to Mineralogy and Petrology* **64,** 205–221.

Arndt, N. T. & Jenner, G. A., (1986). Crustally contaminated komatiites and basalts from Kimbalda, Western Australia. *Chemical Geology* **56,** 229–255.

Arndt, N. T. & Lesher, C. M., (1992). Fractionation of REEs by olivine and the origin of Kambalda komatiites, Western Australia. *Geochimica et Cosmochimica Acta* **56,** 4191–4204.

Arndt, N. T., Naldrett, A. J. & Pyke, D. R., (1977). Komatiitic and iron-rich tholeiitic lavas of Munro Township, Northeast Ontario. *Journal of Petrology* **18,** 319–369.

Arndt, N. T., Kerr, A. C. & Tarney, J., (1997). Dynamic melting in plume heads: the formation of Gorgona komatiites and basalts. *Earth and Planetary Science Letters* **146,** 289–301.

Arth, J. G., Arndt, N. T. & Naldrett, A. J., (1977). Genesis of Archean komatiites from Munro Township, Ontario: trace element evidence. *Geology* **5,** 590–594.

Baker, M. B. & Stolper, E. M., (1994). Determining the composition of high-pressure mantle melts using diamond aggregates. *Geochimica et Cosmochimica Acta* **58,** 2811–2827.

Bertka, C. M. & Holloway, J. R., (1993). Pigeonite at solidus temperatures: implications for partial melting. *Journal of Geophysical Research* **98,** 19755–19766.

Beswick, A. E., (1982). Some geochemical aspects of alteration, and genetic relations in komatiitic suites. In: Arndt, N. T. & Nisbet, E. G. (eds) *Komatiites*. London: George Allen & Unwin, pp. 283–308.

Bickle, M. J., Arndt, N. T., Nisbet, E. G., Orpen, J. L., Martin, A., Keays, R. R. & Renner, R., (1993). Geochemistry of the igneous rocks of the Belingwe Greenstone Belt: alteration, contamination and petrogenesis. In: Bickle, M. J. & Nisbet, E. G. (eds) *The Geology of the Belingwe Greenstone Belt, Zimbabwe: a Study of the Evolution of Archaean Continental Crust*. Rotterdam: A. A. Balkema, pp. 175–214.

Bonatti, E. & Michael, P. J., (1989). Mantle peridotites from continental rifts to ocean basins to subduction zones. *Earth and Planetary Science Letters* **91,** 297–311.

Bonatti, E., Ottonello, G. & Hamlyn, P. R., (1986). Peridotites from the island of Zabargad (St. John), Red Sea: petrology and geochemistry. *Journal of Geophysical Research* **91,** 599–631.

Boyd, F. R., (1984). Siberian geotherm based on lherzolite xenoliths from the Udachnaya kimberlite, USSR. *Geology* **12,** 528–530.

Boyd, F. R., (1989). Compositional distinction between oceanic and cratonic lithosphere. *Earth and Planetary Science Letters* **96,** 15–26.

Boyd, F. R. & England, J. L., (1960). Apparatus for phase equilibrium measurements at pressures up to 50 kilobars and temperatures up to 1750°C. *Journal of Geophysical Research* **65,** 741–748.

Boyd, F. R. & Gurney, J. J., (1986). Diamonds and the African lithosphere. *Science* **232,** 472–477.

Boyd, F. R. & Mertzman, S. A., (1987). Composition and structure of the Kaapvaal lithosphere, southern Africa. In: Mysen, B. O. (ed.) *Magmatic Processes: Physicochemical Principles. Geochemical Society Special Publication* **1,** 13–24.

Boyd, F. R. & Nixon, P. H., (1978). Ultramafic nodules from the Kimberley pipes, South Africa. *Geochimica et Cosmochimica Acta* **42,** 1367–1382.

Boyd, F. R., Pokhilenko, N. P., Pearson, D. G., Mertzman, S. A., Sobolev, N. V. & Finger, L. W., (1997). Composition of the Siberian cratonic mantle: evidence from Udachnaya peridotite xenoliths. *Contributions to Mineralogy and Petrology* **128,** 228–246.

Campbell, I. H., Griffiths, R. W. & Hill, R. I., (1989). Melting in an Archean mantle plume: heads it's basalts, tails it's komatiites. *Nature* **339,** 697–699.

Canil, D., (1991). Experimental evidence for the exsolution of cratonic peridotite from high-temperature harzburgite. *Earth and Planetary Science Letters* **106,** 64–72.

Canil, D., (1992). Orthopyroxene stability along the peridotite solidus and the origin of cratonic lithosphere beneath southern Africa. *Earth and Planetary Science Letters* **111,** 83–95.

Carswell, D. A., Clarke, D. B. & Mitchell, R. H., (1979). The petrology and geochemistry of ultramafic nodules. In: Boyd, F. R. & Meyer, H. O. A. (eds) *The Mantle Sample. Proceedings 2nd International Kimberlite Conference, Vol. 2*. Washington, DC: American Geophysical Union, pp. 127–144.

Cattell, A. & Arndt, N., (1987). Low- and high alumina komatiites from a late Archaean sequence, Newton Township, Ontario. *Contributions to Mineralogy and Petrology* **97,** 218–227.

Cox, K. G., Gurney, J. J. & Harte, B., (1973). Xenoliths from the Matsoku Pipe. In: Nixon, P. H. (ed.) *Lesotho Kimberlites*. Maseru,

Lesotho: Lesotho National Development Corporation, pp. 76–100.

Cox, K. G., Smith, M. R. & Beswetherrick, S., (1987). Textural studies of garnet lherzolites: evidence of probable exsolution origin from fertile harzburgite. In: Nixon, P. H. (ed.) *Mantle Xenoliths*. New York: John Wiley, pp. 537–550.

Danchin, R. V., (1979). Mineral and bulk chemistry of garnet lherzolite and garnet harzburgite xenoliths from the Premier Mine, South Africa. In: Boyd, F. R. & Meyer, H. O. A. (eds) *The Mantle Sample. Proceedings 2nd International Kimberlite Conference, Vol. 2*. Washington, DC: American Geophysical Union, pp. 104–126.

Davis, B. T. C., (1964). The system diopside–forsterite–pyrope at 40 kilobars. *Carnegie Institution of Washington, Yearbook* **63,** 165–171.

Dawson, J. B., Smith, J. V. & Hervig, R. L., (1980). Heterogeneity in upper mantle lherzolites and harzburgites. *Philosophical Transactions of the Royal Society of London, Series A* **297,** 323–331.

Dick, H. J. B., (1989). Abyssal peridotites, very slow spreading ridges and ocean ridge magmatism. In: Saunders, A. D. & Norry, M. J. (eds) *Magmatism in the Ocean Basins. Geological Society, London, Special Publication* **42,** 71–105.

Dick, H. J. B. & Fisher, R. L., (1984). Mineralogic studies of the residues of mantle melting: abyssal and Alpine-type peridotites. In: Kornprobst, J. (ed.) *Kimberlites. The Mantle and Crust–Mantle Relationships*. Amsterdam: Elsevier, pp. 295–308.

Falloon, T. J. & Green, D. H., (1988). Anhydrous partial melting of peridotite from 8 to 35 kb and the petrogenesis of MORB. *Journal of Petrology* Special Lithosphere Issue, 379–414.

Griffin, W. L., O'Reilly, S. Y., Ryan, C. G., Gaul, O. & Ionov, D. A., (1997). Secular variation in the composition of subcontinental lithospheric mantle. *AGU Monograph* **24**. In press.

Grove, T. L., Gaetani, G. A. & deWit, M. J., (1994). Spinifex textures in 3·49 Ga Barberton Mountain belt komatiites: evidence for crystallization of water-bearing, cool magmas in the Archean. *EOS Transactions, American Geophysical Union* **75,** 354.

Gruau, G., Jahn, B. M., Glikson, A. Y., Davy, R., Hickman, A. H. & Chauvel, C., (1987). Age of the Archean Talga-Talga Subgroup, Pilbara Block, Western Australia, and early evolution of the mantle: new Sm–Nd isotopic evidence. *Earth and Planetary Science Letters* **85,** 105–116.

Gudfinnsson, G. H. & Presnall, D. C., (1996). Melting relations of model lherzolite in the system CaO–MgO–Al$_2$O$_3$–SiO$_2$ at 2·4 to 3·4 GPa and the generation of komatiites. *Journal of Geophysical Research* **101,** 27701–27710.

Hallberg, J. A. & Williams, D. A. C., (1972). Archean mafic and ultramafic rock associations in the Eastern Goldfields Region, Western Australia. *Earth and Planetary Science Letters* **15,** 191–200.

Hauri, E. H. & Hart, S. R., (1995). Correction to 'Constraints on melt migration from mantle plumes: a trace element study of peridotite xenoliths from Savai'i, Western Samoa'. *Journal of Geophysical Research* **100,** 2003.

Herzberg, C., (1992). Depth and degree of melting of komatiites. *Journal of Geophysical Research* **97,** 4521–4540.

Herzberg, C., (1993). Lithosphere peridotites of the Kaapvaal craton. *Earth and Planetary Science Letters* **120,** 13–29.

Herzberg, C., (1995). Generation of plume magmas through time: an experimental perspective. *Chemical Geology* **126,** 1–16.

Herzberg, C. & Zhang, J., (1996). Melting experiments on anhydrous peridotite KLB-1: compositions of magmas in the upper mantle and transition zone. *Journal of Geophysical Research* **101,** 8271–8295.

Herzberg, C. & Zhang, J., (1997). Melting experiments on komatiite analog compositions at 5 GPa. *American Mineralogist* **82,** 354–367.

Herzberg, C. & Zhang, J., 1998. Melting experiments in the systems CaO–MgO–Al$_2$O$_3$–SiO$_2$ at 3 to 15 GPa. *American Mineralogist*, submitted.

Herzberg, C., Feigenson, M., Skuba, C. & Ohtani, E., (1988). Majorite fractionation recorded in the geochemistry of peridotites from South Africa. *Nature* **332,** 823–826.

Herzberg, C., Gasparik, T. & Sawamoto, H., (1990). Origin of mantle peridotite: constraints from melting experiments to 16·5 GPa. *Journal of Geophysical Research* **95,** 15779–15803.

Hirose, K. & Kushiro, I., (1993). Partial melting of dry peridotites at high pressures: determination of compositions of melts segregated from peridotite using aggregates of diamond. *Earth and Planetary Science Letters* **114,** 477–489.

Ito, E. & Takahashi, E., (1987). Melting of dry peridotite KLB-1 up to 14 GPa: implications on the origin of peridotitic upper mantle. *Journal of Geophysical Research* **91,** 9367–9382.

Jagoutz, E., Palme, H., Baddenhausen, H., Blum, K., Cendales, K., Dreibus, G., Spettel, B., Lorenz, V. & Wanke, H., (1979). The abundances of major, minor and trace elements in the Earth's mantle as derived from primitive ultramafic nodules. *Proceedings of the 10th Lunar and Planetary Science Conference. Geochimica et Cosmochimica Acta Supplement* 2031–2050.

Jagoutz, E., Dawson, J. B., Hoernes, S., Spettel, B., & Wanke, H., (1984). Anorthositic oceanic crust in the Archean Earth. *Proceedings of the 15th Lunar and Planetary Science Conference. Journal of Geophysical Research Supplement* 395–396.

Jahn, B.-M., Gruau, G. & Glikson, A. Y., (1982). Komatiites of the Onverwacht Group, S. Africa: REE geochemistry, Sm/Nd age and mantle evolution. *Contributions to Mineralogy and Petrology* **80,** 25–40.

Johnson, K. T. M., Dick, H. J. B. & Shimizu, N., (1990). Melting in the oceanic upper mantle: an ion microprobe study of diopsides in abyssal peridotites. *Journal of Geophysical Research* **95,** 2661–2678.

Kato, T., Ringwood, A. E. & Irifune, T., (1988). Experimental determination of element partitioning between silicate perovskites, garnets and liquids: constraints on early differentiation of the mantle. *Earth and Planetary Science Letters* **89,** 123–145.

Kawamoto, T. & Holloway, J. R., (1997). Melting temperature and partial melt chemistry of H_2O-saturated mantle peridotite to 11 GPa. *Science* **276,** 240–243.

Kelemen, P. B. & Hart, S. R., (1996). Silica enrichment in the continental lithosphere via melt rock reaction. *V. M. Goldschmidt Conference, Journal of Conference Abstracts* **1,** 308.

Kelemen, P. B., Dick, H. J. B. & Quick, J. E., (1992). Formation of harzburgite by pervasive melt/rock reaction in the upper mantle. *Nature* **358,** 635–641.

Kesson, S. E. & Ringwood, A. E., (1989). Slab–mantle interactions 2. The formation of diamonds. *Chemical Geology* **78,** 97–118.

Kinzler, R. J., (1997). Melting of mantle peridotite at pressures approaching the spinel to garnet transition: application to mid-ocean ridge basalt petrogenesis. *Journal of Geophysical Research* **102,** 853–874.

Kinzler, R. J. & Grove, T. L., 1992a. Primary magmas of mid-ocean ridge basalts 1. Experiments and methods. *Journal of Geophysical Research* **97,** 6885–6906.

Kinzler, R. J. & Grove, T. L., 1992b. Primary magmas of mid-ocean ridge basalts 2. Applications. *Journal of Geophysical Research* **97,** 6907–6926.

Klein, E. M. & Langmuir, C. H., (1987). Global correlations of mid-ocean ridge basalt chemistry with axial depth and crustal thickness. *Journal of Geophysical Research* **92,** 8089–8115.

Kushiro, I., (1996). Partial melting of a fertile mantle peridotite at high pressures: an experimental study using aggregates of diamond. In: Basu, A. & Hart, S. (ed.) *Earth Processes: Reading the Isotopic Code. Geophysical Monograph, American Geophysical Union* **95,** 109–122.

Lahaye, Y. & Arndt, N., (1996). Alteration of a komatiite flow from Alexo, Ontario, Canada. *Journal of Petrology* **37,** 1261–1284.

Lecuyer, C., Gruau, G., Anhaeusser, C. R. & Fourcade, S., (1994). The origin of fluids and effects of metamorphism on the primary chemical compositions of Barberton komatiites: new evidence from geochemical (REE) and isotopic (Nd, O, H, $^{39}Ar/^{40}Ar$) data. *Geochimica et Cosmochimica Acta* **58,** 969–984.

Lesher, C. E. & Walker, D., (1988). Cumulate maturation and melt migration in a temperature gradient. *Journal of Geophysical Research* **93,** 10295–10311.

Longhi, J. & Bertka, C. M., (1996). Graphical analysis of pigeonite–augite liquidus equilibria. *American Mineralogist* **81,** 685–695.

Maaloe, S. & Aoki, K.-I., (1977). The major element composition of the upper mantle estimated from the composition of lherzolites. *Contributions to Mineralogy and Petrology* **63,** 161–173.

McDonough, W. F. & Sun, S.-S., (1995). The composition of the Earth. *Chemical Geology* **120,** 223–253.

McFarlane, E. A., Drake, M. J. & Rubie, D. C., (1994). Element partitioning between Mg-perovskite, magnesiowustite, and silicate melt at conditions of the Earth's mantle. *Geochimica et Cosmochimica Acta* **58,** 5161–5172.

Milholland, C. S. & Presnall, D. C., (1998). Liquidus phase relations in the CaO–MgO–Al_2O_3–SiO_2 system at 3·0 GPa: the aluminous pyroxene thermal divide and high-pressure fractionation of picritic and komatiitic magmas. *Journal of Petrology* **38,** 3–27.

Mysen, B. O. & Kushiro, I., (1977). Compositional variations of coexisting phases with degree of melting of peridotite in the upper mantle. *American Mineralogist* **62,** 843–865.

Nesbitt, R. W. & Sun, S.-S., (1976). Geochemistry of Archaean spinifex-textured peridotites and magnesian and low-magnesian tholeiites. *Earth and Planetary Science Letters* **31,** 433–453.

Nesbitt, R. W., Sun, S.-S. & Purvis, A. C., (1979). Komatiites: geochemistry and genesis. *Canadian Mineralogist* **17,** 165–186.

Nisbet, E. G., Arndt, N. T., Bickle, M. J., Cameron, W. E., Chauvel, C., Cheadle, M., Hegner, E., Kyser, T. K., Martin, A., Renner, R. & Roedder, E., (1987). Uniquely fresh 2·7 Ga komatiites from the Belingwe greenstone belt, Zimbabwe. *Geology* **15,** 1147–1150.

O'Hara, M. J., (1968). The bearing of phase equilibria studies in synthetic and natural systems on the origin and evolution of basic and ultrabasic rocks. *Earth-Science Reviews* **4,** 69–134.

O'Hara, M. J. & Yoder, H. S., (1967). Formation and fractionation of basic magmas at high pressures. *Scottish Journal of Geology* **3,** 67–117.

Ohtani, E., Kawabe, I., Moriyama, J. & Nagata, Y., (1989). Partitioning of elements between majorite garnet and melt and implications for petrogenesis of komatiite. *Contributions to Mineralogy and Petrology* **103,** 263–269.

Pearson, D. G., Carlson, R. W., Shirey, S. B., Boyd, F. R., Nixon, P. H. & Pokhilenko, N. P., 1995a. Stabilization of Archean lithospheric mantle: a Re–Os isotopic study of peridotite xenoliths from the Kaapvaal craton. *Earth and Planetary Science Letters* **134,** 341–357.

Pearson, D. G., Shirey, S. B., Carlson, R. W., Boyd, F. R., Pokhilenko, N. P. & Shimizu, N., 1995b. Re–Os, Sm–Nd, and Rb–Sr isotopic evidence for thick Archean lithosphere mantle beneath the Siberian craton modified by multistage metasomatism. *Geochimica et Cosmochimica Acta* **59,** 959–978.

Presnall, D. C., Dixon, S. A., Dixon, J. R., O'Donnell, T. H., Brenner, N. L., Schrock, R. L. & Dycus, D. W., (1978). Liquidus phase relations on the join diopside–forsterite–anorthite from 1 atm. to 20 kbar: their bearing on the generation and crystallization of basaltic magma. *Contributions to Mineralogy and Petrology* **66,** 203–220.

Presnall, D. C., Weng, Y.-H., Milholland, C. S. & Walter, M. J., (1997). Liquidus phase relations in the system MgO–$MgSiO_3$ at pressures up to 25 GPa—constraints on crystallization of a molten Hadean mantle. *Physics of Earth and Planetary Interiors* (in press).

Press, W. H., Teukolsky, S. A., Vetterling, W. T. & Flannery, B. P., (1992). *Numerical Recipes in FORTRAN: the Art of Scientific Computing*, 2nd edn. Cambridge: Cambridge University Press, 963 pp.

Rudnick, R. L., McDonough, W. F. & Orpin, A., (1994). Northern Tanzanian peridotite xenoliths: a comparison with Kaapvaal peridotites and inferences on metasomatic interactions. In: Meyer, H. O. & Leonardos, O. H. (eds) *Kimberlites, Related Rocks and Mantle Xenoliths. Proceedings 5th International Kimberlite Conference, Vol. 1*, Rio de Janeiro: CPRM, pp. 336–354.

Russell, J. K., Nicholls, J., Stanley, C. R. & Pearce, T. H., (1990). Pearce element ratios: a paradigm for testing hypotheses. *EOS Transactions, American Geophysical Union* **71**, 234–236, 246–247.

Smith, H. S. & Erlank, A. J., (1982). Geochemistry and petrogenesis of komatiites from the Barberton greenstone belt, South Africa. In: Arndt, N. T. & Nisbet, E. G. (eds) *Komatiites*. London: George Allen & Unwin, pp. 347–397.

Stone, W. E., Deloule, E., Larson, M. S. & Lesher, C. M., (1997). Evidence for hydrous high-MgO melts in the Precambrian. *Geology* **25**, 143–146.

Sun, S.-S. & Nesbitt, R. W., (1978). Petrogenesis of Archaean ultrabasic and basic volcanics: evidence from rare earth elements. *Contributions to Mineralogy and Petrology* **65**, 301–325.

Takahashi, E., (1986). Melting of a dry peridotite KLB-1 up to 14 GPa: implications on the origin of peridotitic upper mantle. *Journal of Geophysical Research* **91**, 9367–9382.

Takahashi, E., (1990). Speculations on the Archean mantle: missing link between komatiite and depleted garnet peridotite. *Journal of Geophysical Research* **95**, 15941–15954.

Takahashi, E. & Scarfe, C. M., (1985). Melting of peridotite to 14 GPa and the genesis of komatiite. *Nature* **315**, 566–568.

Takahashi, E., Shimazaki, T., Tsuzaki, Y. & Yoshida, H., (1993). Melting study of peridotite KLB-1 to 6·5 GPa, and the origin of basaltic magmas. *Philosophical Transactions of the Royal Society of London* **342**, 105–120.

Walker, R. J., Carlson, R. W., Shirey, S. B. & Boyd, F. R., (1989). Os, Sr, Nd, and Pb isotopic systematics of southern African peridotite xenoliths: implications for the chemical evolution of subcontinental mantle. *Geochimica et Cosmochimica Acta* **53**, 1583–1595.

Walter, M. J. & Presnall, D. C., (1994). Melting behavior of simplified lherzolite in the system CaO–MgO–Al₂O₃–SiO₂–Na₂O from 7 to 35 kbar. *Journal of Petrology* **35**, 329–359.

Walter, M. J., Sisson, T. W. & Presnall, D. C., (1995a). A mass proportion method for calculating melting reactions and application to melting of model upper mantle lherzolite. *Earth and Planetary Science Letters* **135**, 77–90.

Walter, M. J., Thibault, Y., Wei, K. & Luth, R. W., (1995b). Characterizing experimental pressure and temperature conditions in multi-anvil apparatus. *Canadian Journal of Physics* **73**, 273–286.

Wei, K., Tronnes, R. & Scarfe, C. M., (1990). Phase relations of aluminum-undepleted and aluminum-depleted komatiites at pressures of 4–12 GPa. *Journal of Geophysical Research* **95**, 15817–15827.

Wetherill, G. W., (1985). Occurrence of giant impacts during the growth of the terrestrial planets. *Science* **228**, 877–879.

Williams, D. A. C. & Furnell, R. G., (1979). Reassessment of part of the Barberton Type Area, South Africa. *Precambrian Research* **9**, 325–347.

Wilson, M., (1989). *Igneous Petrogenesis*. London: Unwin Hyman, 466 pp.

Xie, Q., Kerrich, R. & Fan, J., (1993). HFSE/REE fractionations recorded in three komatiite–basalt sequences, Archean Abitibi greenstone belt: implications for multiple plume sources and depths. *Geochimica et Cosmochimica Acta* **57**, 4111–4118.

Xue, X., Baadsgaard, H., Irving, A. J. & Scarfe, C. M., (1990). Geochemical and isotopic characteristics of lithospheric mantle beneath West Kettle River, British Columbia: evidence from ultramafic xenoliths. *Journal of Geophysical Research* **95**, 15879–15891.

Yoder, H. S. J., (1976). *Generation of Basaltic Magma*. Washington, DC: National Academy of Sciences, 265 pp.

Zhang, J. & Herzberg, C., (1994). Melting experiments on anhydrous peridotite KLB-1 from 5·0 to 22·5 GPa. *Journal of Geophysical Research* **99**(B9), 17729–17742.